INFORMATION TO USERS

This manuscript has been reproduced from the microfilm master. UMI films the text directly from the original or copy submitted. Thus, some thesis and dissertation copies are in typewriter face, while others may be from any type of computer printer.

The quality of this reproduction is dependent upon the quality of the copy submitted. Broken or indistinct print, colored or poor quality illustrations and photographs, print bleedthrough, substandard margins, and improper alignment can adversely affect reproduction.

In the unlikely event that the author did not send UMI a complete manuscript and there are missing pages, these will be noted. Also, if unauthorized copyright material had to be removed, a note will indicate the deletion.

Oversize materials (e.g., maps, drawings, charts) are reproduced by sectioning the original, beginning at the upper left-hand corner and continuing from left to right in equal sections with small overlaps.

ProQuest Information and Learning
300 North Zeeb Road, Ann Arbor, MI 48106-1346 USA
800-521-0600

Direct Initiation of Detonations with Multi-Step Reaction Scheme

by

Hoi Dick Ng

Department of Mechanical Engineering
McGill University
Montréal, Québec, Canada

A thesis submitted to the
Faculty of Graduate Studies and Research
in partial fulfillment of the requirements for the degree of
Master's in Engineering

January 2001

Abstract

The problem of direct initiation of detonations has been investigated numerically by using a more realistic chemical kinetics scheme. The chemical kinetics model is based on a three-step chain-branching reaction consists sequentially of a chain-initiation and a chain-branching step, followed by a temperature independent chain-termination. The steady ZND structure using the 3-step chemical kinetics model is compared with that based on the standard single-step Arrhenius rate model. The 3-step chemical kinetics model is shown to permit an independent variation of the induction and reaction zone length and a number of different steady-state detonation profiles can be derived. An unsteady computation has also been performed to determine whether the solution from steady-state analysis can be approached asymptotically from a transient development. Oscillatory or even chaotic detonations are observed for high values of the ratio between the induction and reaction zone length, which is a more adequate parameter to characterize the stability of detonation waves. The transient results also show that the present multi-step kinetics model provides a chemical switch-off mechanism that causes detonation failure, which cannot be described by using a single-step Arrhenius rate law.

The three regimes of direct initiation have been numerically simulated for planar, cylindrical and spherical geometries using the present 3-step chemical kinetics model. The use of a more realistic reaction scheme allows a unique value for the critical initiation energy to be defined. The numerical results demonstrate that detonation instability plays an important role in the initiation process. The effect of curvature for cylindrical and spherical geometries has been found to enhance the instability of the detonation waves and thus influences the initiation process.

Some general theories for direct initiation have been verified from the results of the present numerical simulation using a more detailed chemical kinetics model, where a definitive value of the critical energy was obtained. It was found that these theories are satisfactory only for stable detonation waves and start to break down for highly unstable detonations because they are based on simple blast wave theory and do not include a parameter to model the detonation instability. This study suggests that a stability parameter, such as the ratio between the induction and reaction zone length, should be considered in the future development of a more rigorous theory for direct initiation.

Résumé

Le problème de l'initiation directe des détonations a été étudié numériquement en utilisant un schéma de cinétique chimique plus réaliste. Ce schéma réactionnel est basé sur une réaction "chain-branching" à trois étapes, qui consiste, séquentiellement, en une étape "chain-initiation" et une étape "chain-branching", suivies d'une étape "chain-termination" indépendante de la température. La structure ZND stationnaire obtenue grâce à ce schéma réactionnel à trois étapes est comparée avec celle basée sur une réaction de type Arrhenius à une seule étape. Le schéma réactionnel à trois étapes permet une variation indépendante des longueurs des zones d'induction et de réaction, et une multitude de profils thermodynamiques stationnaires différents peuvent être obtenus. Des calculs instationnaires peuvent aussi être réalisés pour déterminer si la solution du calcul stationnaire peut être approchée asymptotiquement à partir d'un développement instationnaire. Des détonations oscillatoires et même chaotiques sont observées pour des valeurs élevées du rapport entre les longueurs d'induction et de réaction, qui représente un paramètre plus adéquat pour caractériser la stabilité des ondes de détonation. Les résultats instationnaires démontrent aussi que le présent schéma multi-réactionnel permet un mécanisme d'extinction de la détonation, ce qui ne peut être expliqué grâce à un schéma réactionnel Arrhenius à une seule étape.

Les trois régimes d'initiation directe ont été simulés numériquement pour des géométries planaire, cylindrique et sphérique à partir du présent schéma multi-réactionnel. L'utilisation d'un schéma plus réaliste permet de déterminer une valeur unique de l'énergie critique d'initiation. A partir des simulations numériques, il est démontré que l'instabilité des détonations joue un rôle important dans le processus d'initiation. Il a été démontré que l'effet de courbure pour les géométries cylindrique et sphérique augmente l'instabilité de l'onde de détonation et influence donc le processus d'initiation.

Certaines théories générales de l'initiation des détonations ont été vérifiées à partir des résultats de la présente simulation basée sur un schéma multi-réactionnel, où une valeur bien définie de l'énergie critique d'initiation est obtenue. Il appert que ces théories sont satisfaisantes uniquement pour les détonations stables. Ces théories échouent pour les détonations hautement instables, puisque qu'elles sont basées sur la théorie simple des ondes de souffle, et n'incluent pas de paramètre pour décrire l'instabilité des détonations. La présente étude suggère qu'un paramètre de stabilité, tel que le rapport entre la longueur des zones d'induction et de réaction, pourrait être considéré dans le développement futur d'une théorie plus rigoureuse pour l'initiation directe des détonations.

Acknowledgments

I would like to sincerely thank my supervisor, Prof. John H.S. Lee, for giving me the opportunity to work with the McGill Shock Wave Physic Group (SWPG) and also for his helpful hints, availability and guidance throughout my graduate studies. A special thank to Dr. Jean-Philippe Dionne, who taught me so many things on the field of detonation physics and helped me to translate the abstract into French. Many thanks are also due to Dr. Randy Chue for his valuable advice and assistance and to Dr. Kiumars Mazaheri for allowing me to use his detonation code. I am grateful to Prof. Andrew Higgins for his comments and fruitful discussions on the preparation of the final version of this thesis. The assistance from all members of the Shock Wave Physics Group is gratefully acknowledged. I also want to extend my full gratitude to my family, all my friends, brothers and sisters in Enoch Fellowship of Montreal Chinese Alliance Church for their support and encouragement. Finally, I would like to acknowledge the Natural Sciences and Engineering Research Council of Canada (NSERC) for their financial support.

Table of Contents

List of Figures

List of Tables

Nomenclature

c_0	sound speed in the unburned mixture
e	total internal energy
E_s	source energy
E_s^*	critical initiation energy
E_I	activation energy of the initiation step
E_B	activation energy of the chain branching step
F	fuel species
f	mass fraction of fuel
H	specific enthalpy
j	geometric index (j=0, 1, 2 for planar, cylindrical and spherical)
k_I	rate constant of the initiation step
k_B	rate constant of the chain branching step
k_C	rate constant of the chain termination step
M_s	shock Mach number
M_s^*	critical shock Mach number
P	pressure
Q	total chemical heat release
r	distance coordinate
r_c	characteristic length scale
R_0	explosion length
R_s	shock radius
R_s^*	critical radius
T	temperature
t	time
t_c	characteristic time scale
u	particle velocity
v	specific volume

w_i	reaction rate of the initiation step
w_B	reaction rate of the chain branching step
w_c	reaction rate of the chain termination step
Y	radical species
y	mass fraction of radicals

Acronyms

CJ	Chapman-Jouguet
DDT	Deflagration to Detonation Transition
SWACER	Shock Wave Amplification by Coherent Energy Release
VN	Von Neumann
ZND	Zel'dovich- Von Neumann- Döring

Greek

α_i	blast wave constant
Δ_i	induction zone length
Δ_R	reaction zone length
δ	ratio between induction and reaction zone length
γ	ratio of specific heats
λ	detonation cell size
ρ	density
ρ_o	initial density

Subscripts

L	left
R	right
o	initial condition, unburnt mixture properties
sh	post-shock condition

Chapter 1

Introduction

There are two modes of combustion in general: deflagration and detonation. Detonation is a supersonic combustion wave that propagates via auto-ignition from adiabatic shock compression in contrast with slow deflagration whose propagation depends on heat diffusion and mass transport. Generally, a detonation can be formed in two ways. One way involves the acceleration of a flame, which eventually results in the transition to a detonation under appropriate boundary conditions. This is usually referred to as *deflagration to detonation transition (DDT)*. Alternatively, the other mode of initiation is when the detonation is formed instantaneously from the asymptotic decay of the strong blast wave generated by a rapid deposition of a large amount of energy into the combustible mixture. This mode of initiation is usually referred to as *direct* or *blast initiation*. This thesis focuses mainly on the direct initiation of detonation.

In the limit of an ideal instantaneous point source energy, the ignition energy becomes the sole parameter that determines the possible outcome of the initiation process, i.e., whether a detonation can be initiated or not. If, for given experimental condition, a sufficiently large amount of energy is released by the igniter, then the blast wave will decay asymptotically to the Chapman-Jouguet (C-J) velocity of the combustible mixture. A self-sustained detonation is thus successfully initiated. If the igniter energy is too low, the initiation of detonation fails. In this case, the blast wave generated by the igniter will progressively decouple from the reaction zone and eventually decays to a weak shock wave. A critical threshold value for the initiation energy can be identified below which no detonation can be formed. This minimum energy required to successfully initiate a detonation is usually referred to as the *critical initiation energy*.

Over the past four decades, direct initiation of detonation has been a subject of intense study. Since the pioneer work of Zel'dovich *et al.* [42], significant advances have been made toward the understanding of direct initiation phenomenon. Numerous studies were carried out which attempted to yield a predictive theory for the critical initiation energy. In spite of all these efforts, a quantitative theory capable of predicting the critical energy from first principles based on thermo-chemical and chemical kinetics data of the mixture is still lacking. Moreover, the weakest parts of previous theoretical and numerical investigations on direct initiation is their sub-model for chemical kinetics. Most of these investigations are based on an idealized single-step Arrhenius rate law to model the chemistry. Although the use of single-step Arrhenius kinetics model simplifies the analysis and reveals some interesting global features of the phenomenon, it does not describe the realistic reaction scheme of most explosive mixtures. Hence, the results obtained are not even in qualitative agreement with some experimental observations. For instance, in the numerical study by Mazaheri [30], it was demonstrated that a single-step Arrhenius rate law is not an adequate chemical kinetics model for the problem of direct initiation due to the difficulty in defining a unique value of critical initiation energy. For single-step chemistry, a system without losses will always react to completion. Hence initiation will always occur after a sufficiently long time and a critical value of initiation energy no longer exists. This often yields the non-physical result that initiation of detonation can always be achieved via any arbitrary strength of shock wave.

Recent studies have revealed that detailed chemical kinetics steps are also able to influence the initiation and propagation of the detonation wave, as well as the detonation structure. Dionne [13] studied the propagation of non-ideal detonations arising from reaction steps involving a competition between exothermic and endothermic reactions. It was found that the propagation of detonation could be different by using more than one single-step rate law. Dionne reported that pathological detonations, i.e., detonations can travel at a velocity faster than the Chapman Jouguet value, are possible when there are more than one-step kinetics present in the chemical model.

Dold & Kapila [15] have investigated the difference between shock initiation of detonation based on an asymptotic analysis using a global one-step model and a three-step chain-branching chemical model. They found that the development of detonation behind an initiating shock wave is fundamentally different when the chemistry is modeled using a radical chain-branching mechanism from that of using a global one-step model. Their analyses show that a one-step model is probably not adequate for the study of detonation initiation in combustible mixtures, which are typically burned via a radical chain-branching process.

More recently, Short & Quirk [36] have studied the non-linear stability of a pulsating detonation using the same three-step chain-branching reaction model as in the work of Dold & Kapila [15]. They showed that similar mechanisms for the regular and irregular modes of instability for both the three-step reaction model and the standard one-step reaction model. However, the use of the three-step chain-branching reaction has a distinct advantage over the standard one-step Arrhenius model because a well-defined detonability limit can now be obtained.

In view of the different qualitative features obtained from these studies where a more detailed chemical kinetics is used, it appears of interest to investigate the direct initiation problem using again more realistic chemical kinetics model. Therefore, the main objective of this thesis is to elucidate further the direct initiation phenomenon and investigate the importance of the chemical kinetics scheme used. The motivation for such an investigation is to contribute toward the development of a rigorous theory of direct initiation.

The present investigation was carried out via numerical simulations. A number of numerical schemes are now available [7], which are capable of reproducing many aspects of the highly transient and unstable events of the initiation and propagation of gaseous detonation. Numerical simulations can provide a lot of information, which is difficult to obtain from actual experiments. Although a complex set of kinetics rate equations could in principle be solved simultaneously with the reactive Euler equations within current computational capabilities, it suffices to use a simplified system of three-step reaction

mechanism to just reproduce the qualitative aspects of the initiation phenomenon [27]. In the present study, the same three-step chain-branching reaction model as in the work of Dold & Kapila [15] and Short & Quirk [36] is used to simulate the direct initiation phenomenon. This model consists of a chain-initiation and a chain-branching step, followed by a temperature independent chain-termination. It can represent a generic three-step chemical-kinetics description of a real chain-branching reaction.

The thesis is divided into five Chapters. In Chapter 2, the chemical kinetics model and the governing equations of the problem are first discussed in detail. To demonstrate the effect of the kinetics rate model on detonation, the steady ZND structure using a 3-step chemical kinetics model is investigated and comparison is made with the structure obtained from a single Arrhenius rate law. A transient computation is also carried out to determine whether the solution from the steady state analysis can be approached asymptotically. The instability of detonation waves observed from the fully unsteady computation and its dependence on the chemical kinetics rate model are also discussed. The regimes of direct initiation are then simulated numerically in Chapter 3 for different geometries of planar, cylindrical and spherical case. The effect of detonation instability and the curvature effect on initiation are investigated, followed by a discussion on the existence of a unique value of critical initiation energy with the present 3-step chemical kinetics scheme. In Chapter 4, some general theories for direct initiation are verified through the present numerical results. Finally, the thesis is ended by some concluding remarks in Chapter 5.

Chapter 2

The Detonation Structure

2.1 Introduction

Before we investigate the dependence of the direct initiation process on the details of the chemical kinetics model. it is worthwhile to first examine the steady ZND detonation structure using different chemical kinetics models. We shall first consider the steady ZND structure using a 3-step chemical kinetics model and compare the qualitative differences from that based on the standard single-step Arrhenius rate model used in most theoretical studies. An unsteady analysis is also carried out to verify the existence of the steady-state detonation from an initial transient development and elucidate the nonlinear instability of the one-dimensional detonation wave.

2.2 Analytical model

The dynamics of unsteady propagation of a one-dimensional detonation can be described by the one-dimensional reactive Euler equations. i.e.. a set of hyperbolic partial differential equations in space (in laboratory frame) and time that express the conservation of mass, momentum and energy. They have the following non-dimensional form:

$$\frac{\partial \rho}{\partial t}+\frac{\partial(\rho u)}{\partial r}+\frac{j}{r}(\rho u)=0$$

$$\frac{\partial(\rho u)}{\partial t}+\frac{\partial}{\partial r}\left(\rho u^{2}+p\right)+\frac{j}{r}\left(\rho u^{2}\right)=0$$

$$\frac{\partial(\rho e)}{\partial t}+\frac{\partial}{\partial r}[u(\rho e+p)]+\frac{j}{r}[u(\rho e+p)]=0 \qquad (2.1)$$

where ρ, u, p and e denote the fluid density, velocity, pressure and internal energy respectively. The parameter j represents the geometric factor with $j = 0, 1, 2$ in the planar, cylindrical and spherical geometry. Assuming a perfect gas with constant specific heat ratio γ, the internal energy is defined as:

$$e = \frac{p}{(\gamma - 1)\rho} - q + \frac{1}{2}u^2 \tag{2.2}$$

where q is the local chemical energy release. All the flow variables are non-dimensionalized with respect to the unburned mixture properties (e.g., the density is non-dimensionalized with ρ_0, pressure with γP_0 and the velocity with the sound speed of the unburned mixture c_0).

The chemical kinetics scheme used for the present study is a generalized three-step chain-branching reaction model, which is the same as the one employed by Short & Quirk [36] in their recent investigation of the behavior of pulsating detonation waves. This model involves two temperature-sensitive radical producing reactions and a temperature-independent exothermic chain-termination reaction. It can be represented by the following three main-stages:

1. Initiation	$F \rightarrow Y$	$k_I = \exp\left(E_I\left(\frac{1}{T_I} - \frac{1}{T}\right)\right)$
2. Chain branching	$F + Y \rightarrow 2Y$	$k_B = \exp\left(E_B\left(\frac{1}{T_B} - \frac{1}{T}\right)\right)$
3. Chain termination	$Y \rightarrow P$	$k_C = 1$

(2.3)

where F, Y and P correspond to the amount of reactants, radicals and products, respectively. The chain-initiation and chain-branching rate constants k_I and k_B have an Arrhenius temperature-dependent form $e^{-E/RT}$. The chain-termination reaction or recombination is assumed to be first order, independent of temperature and has a fixed rate constant k_C. The initiation step has the activation energy E_I and the activation energy for the chain-branching step is represented by E_B. The parameters T_I and T_B denote respectively the chain-initiation and chain-branching "cross-over" temperatures. These are the temperatures limits at which the chain-

initiation and chain- branching rates become as fast as the chain-termination rate. To represent typical chain-branching reactions, these different parameters should be within the following limits as mentioned in the paper by Short & Quirk [36]:

$$T_I > T_{shock},\ T_B < T_{shock} \text{ and } E_I >> E_B$$

For the initiation process (step 1), the cross-over temperature T_I is greater than the post shock temperature T_{shock} and it generally has a large activation energy E_I because a large amount of energy is required to break the relatively strong chemical bonds of the reactants. As a result, this reaction step tends to be uniformly slow. This energetically demanding reaction step produces a small concentration of chain carriers from the reactant. As for the chain-branching reaction (step 2), the activation energy is relatively small as compared to E_I. The cross-over temperature T_B is lower than the post shock temperature because once the shock raises the temperature above T_B, chain-branching will have a rapid reaction rate if a sufficient concentration of free radical has been reached. This reaction leads to the rapid growth in the concentration of chain carriers. Finally, the last step (step 3) is an exothermic termination reaction in which chain carriers are converted into products.

In the present study, the reference length scale r_c is chosen such that the chain-termination rate constant is unity, i.e., $k_C = 1$. The reference time scale t_c is set to the reference length scale dividing it with the sound speed of the reactant (i.e., $t_c = r_c/c_o$). Thus all length and time scales are based on the ratios of the recombination time and length.

Denoting the variable f and y to be the mass fraction of the fuel F and radical Y, the consumption equations for fuel and radical can be written as:

$$\frac{\partial(\rho f)}{\partial t} + \frac{\partial(\rho u f)}{\partial r} + \frac{j}{r}(\rho u f) = -w_I - w_B$$

$$\frac{\partial(\rho y)}{\partial t} + \frac{\partial(\rho u y)}{\partial r} + \frac{j}{r}(\rho u y) = w_I + w_B - w_C \qquad (2.4)$$

where:

$$w_I = f \exp\left(E_I \left(\frac{1}{T_I} - \frac{1}{T} \right) \right), \qquad w_B = \rho\, fy \exp\left(E_B \left(\frac{1}{T_B} - \frac{1}{T} \right) \right), \qquad w_C = y \tag{2.5}$$

The local chemical energy release can be written as:

$$q = Q - f \cdot Q - y \cdot (Q + Q_{\text{endo.}}) \tag{2.6}$$

where Q is the total amount of energy released by the fuel and $Q_{\text{endo.}}$ represents the amount of endothermic energy absorbed by the initiation and chain-branching reactions because energy is required to break the bond and dissociate the reactant into free radicals. In the present study, $Q_{\text{endo.}}$ is set to zero for simplicity without loss of generality.

Using the above described chemical kinetics model, four parameters can be adjusted, namely E_I, E_B, T_I and T_B. These parameters can indeed control the ratio of the chain-branching induction length to the length of the recombination zone. It should be noted that it is possible to derive a number of different steady detonation profiles under the ordered limits allowed by the parameters. This model has an advantage over the standard single-step rate law because it allows the variation of the two important length scales of the reaction, namely the induction and reaction zone length. Here, value of Q = 10, E_I = 20, E_B = 8, T_I = $3T_{\text{shock}}$ and γ = 1.2 are used throughout, unless specified otherwise.

2.3 Steady ZND structure

The Zel'dovich-Von Neumann-Döring (ZND) detonation structure is the classical one-dimensional steady structure for a detonation wave, consisting of a normal shock wave followed by an induction zone and a reaction zone (figure 2.1). The termination of the reaction zone is the C-J or sonic plane, where equilibrium occurs. The variation of the state variables in the detonation structure can be obtained via the integration of the three conservation equations together with the chemical kinetics rate law.

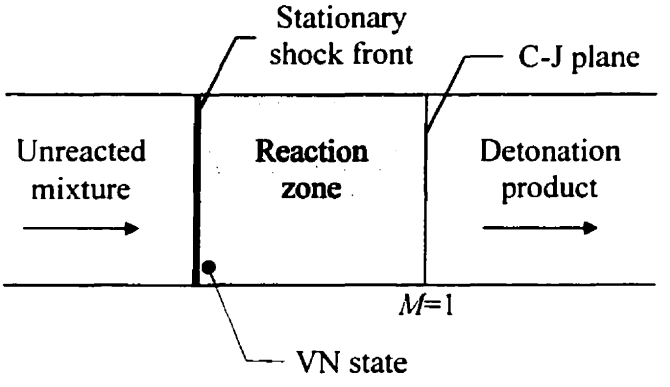

Figure 2.1: One-dimensional ZND detonation structure.

The non-dimensional steady state conservation equations for a coordinate system fixed with respect to the shock front can be written as:

$$M = \frac{u}{v} \qquad \textit{Conservation of mass}$$

$$\frac{1}{\gamma} + M^2 = p + \frac{u^2}{v} = p + Mu \qquad \textit{Conservation of momentum}$$

$$\frac{1}{\gamma - 1} + \frac{M^2}{2} = \frac{\gamma\, pv}{\gamma - 1} + \frac{u^2}{2} - (Q - f \cdot Q - y \cdot Q) \qquad \textit{Conservation of energy}$$

(2.7)

and the variation in fuel and radical concentrations is determined by the following equations:

$$f_r = -(w_I + w_B)/u \quad , \quad y_r = (w_I + w_B - w_C)/u$$

(2.8)

where the subscript r denotes the derivative with respect to the distance r. Detailed derivations of the above equations are given in Appendix I. The above system of equations can be integrated using the initial condition of the shocked state (or Von Neumann state). For a given shock Mach number, the Von Neumann state can be obtained from the Rankine-Hugoniot relationship for a normal shock wave. The integration proceeds until the equilibrium C-J conditions are reached. The possible paths of integration along the Rayleigh line for different shock strengths are shown on the p-v diagram (figure 2.2).

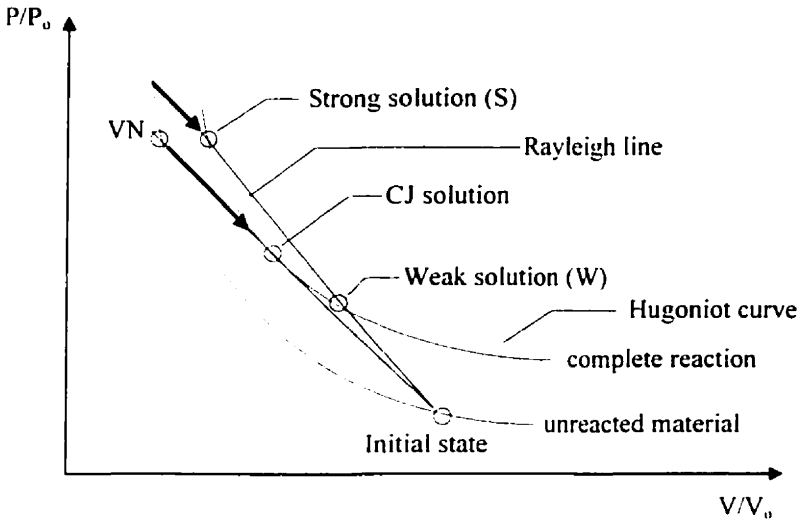

Figure 2.2: p-v diagram showing possible paths of integration.

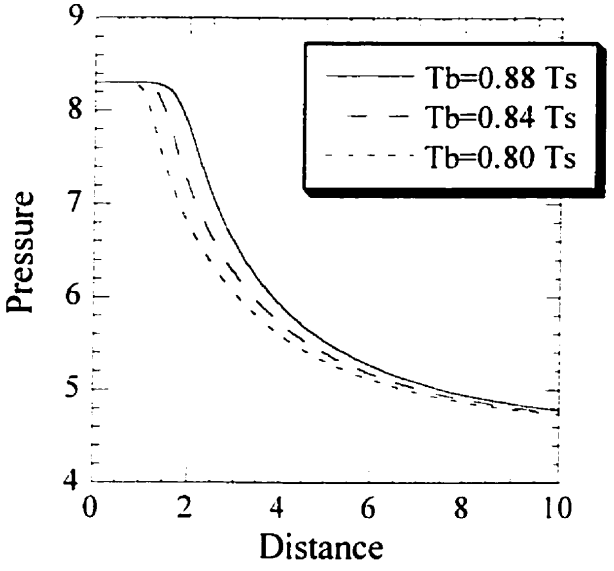

(a)

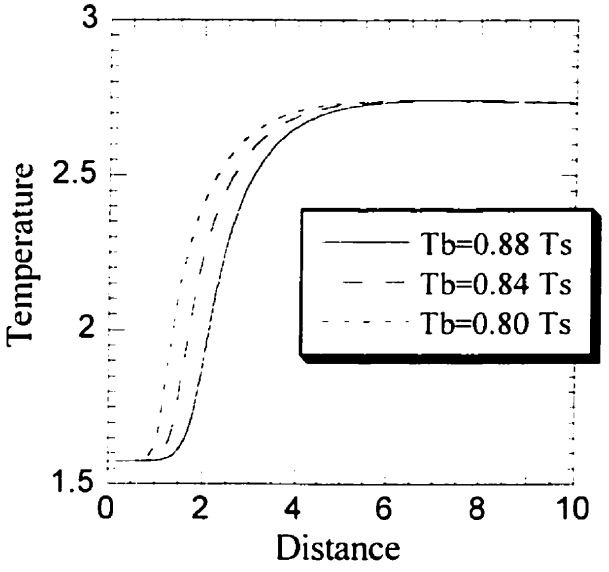

(b)

Figure 2.3: Steady ZND detonation profiles: (a) pressure profile (b) temperature profile for mixture with $Q = 10$, $\gamma = 1.2$, $E_I = 20$, $E_B = 8$ and $T_I = 3T_{shock}$.

Typical pressure and temperature profiles for the ZND structure are illustrated in figures 2.3a and 2.3b. Across the shock, the pressure and temperature jump abruptly to the Von Neumann state. During the induction period both the pressure and temperature remain relatively constant. When energy starts to release in the reaction zone, the pressure drops while the temperature increases. At the end of the reaction zone, the products are at equilibrium and the final state corresponds to values from the C-J solution, if the correct shock velocity is used. From figure 2.3, two distinct regions can be clearly recognized after the shock front, i.e., induction zone and reaction zone. In the induction zone where the "incubation" process occurs, the reactants start to dissociate into free radicals. The free radicals then participate in the exothermic recombination process when the chemical energy is released and temperature increases.

As mentioned previously, the chain-branching cross-over temperature T_B controls the ratio of the induction length to the recombination length. In figure 2.3, T_B varies from $0.80T_{shock}$ to $0.88T_{shock}$ while the other parameters are held constant. By increasing parameter T_B, the induction zone length increases relative to the recombination zone. This can be shown more clearly if we look at the profiles for the consumption of reactant as well as the formation of product.

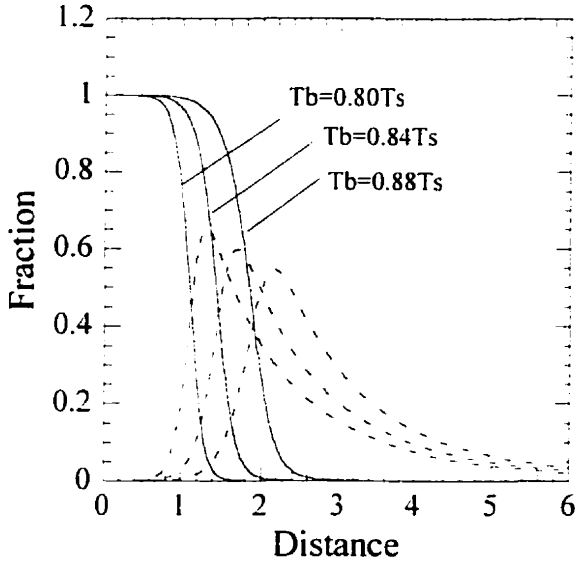

(a)

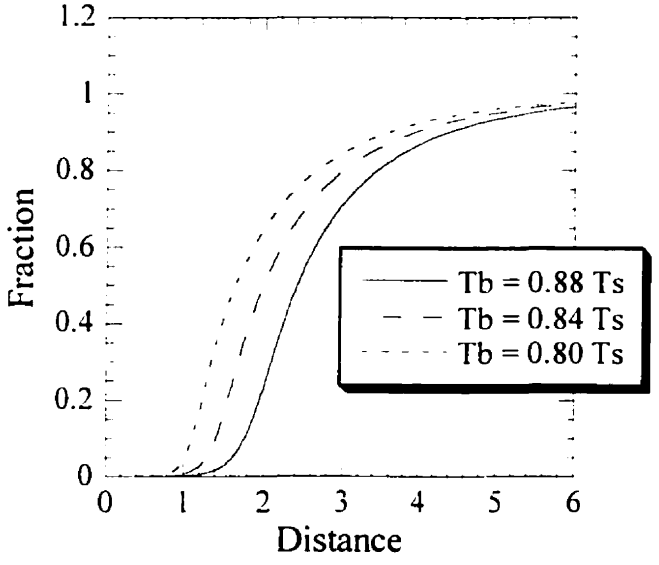

(b)

Figure 2.4: Steady ZND detonation profiles: (a) mass fraction of fuel (solid line) and radicals (dashed line) (b) formation of product for mixture with $Q = 10$, $\gamma = 1.2$, $E_1 = 20$, $E_B = 8$ and $T_1 = 3T_{shock}$.

Figure 2.4 shows the mass fraction of fuel, radical and product profiles in the reaction zone behind the shock front. For a low value of $T_B = 0.80T_{shock}$, the chain-branching induction zone length is small and a significant build up of chain radical concentration occurs rapidly. Since the chain-branching cross-over temperature T_B is the temperature at which the chain-branching rate is equal to that of the chain-termination, we see that for a low value of T_B, the chain-branching reaction rate is significantly greater than that of the recombination reaction and a relatively longer recombination region is obtained before the final equilibrium is reached. However, for higher values of T_B, the chain-branching induction zone increases, resulting in a lower peak concentration of chain radicals. For high values of T_B, the rate of chain-branching reaction is lower, thus allowing the chain-termination reaction to become effective before all the fuel is depleted. Hence, this restricts the build up in free radical concentration in the reaction zone.

From the steady ZND analysis, it is shown that the present three-step model allows us to vary the ratio between the induction zone length and reaction zone length independently. This is one of the distinct advantages over the standard one-step Arrhenius kinetics model. In fact, it is difficult to define an induction zone length in the one-step Arrhenius rate model where both induction and reaction length are governed by a global activation energy.

2.4 Transient computation

The steady state ZND detonation structure has been described in the previous section. However, it is well known that a steady ZND solution may be unstable and the response of the steady-state solution to small perturbations can be obtained via an additional linear stability analysis as those carried out by Lee & Stewart [24] and Sharpe [34]. Alternatively, the stability of a steady-state solution can be studied through an unsteady calculation from initial conditions, where the transient behavior of the detonation is considered. Unsteady numerical simulations of 1-D detonations subject to the present 3-step kinetics model have already been performed by Short & Quirk [36] to study the non-linear stability of the structure of detonation waves. However, they first assumed a stable ZND structure based on the steady-state solution using the C-J criterion, and then subjected this stable solution to a perturbation. It is not clear that the stable ZND profile for the present 3-step chemical kinetics model imposed by Short & Quirk as a starting condition in their simulations can in fact be reached during the transient development of the detonation wave from an arbitrary initiation condition. It is thus important to first examine if the steady detonation using the present 3-step chemical kinetics model can indeed be formed from arbitrary initial conditions before actually focusing on the problem of direct initiation of detonation. In this section, an unsteady analysis of the transient development of a 1-D detonation initiated by a strong blast wave is carried out to determine the existence of the steady detonation wave subject to the present 3-step chemical kinetics model. It is also possible to illustrate the detonation instability and its dependence on the chemical kinetics model from the complete history of the transient development of the detonation initiated by a strong blast wave.

The unsteady one-dimensional reactive Euler equations with the present chemical kinetics scheme are solved numerically using an Eulerian detonation code based on the piecewise parabolic method (PPM) of Colella & Woodward [12], which is a higher order extension of Godunov's method, together with a conservative shock front tracking algorithm [9]. Due to the small length scale of the present problem, it is important to properly refine the reaction zone.

Therefore, an adaptive mesh refinement is used [2]. The computation domain is covered by an uniform coarse grid of 20 numerical cells per half-reaction zone length. An extra fine grid is used, with a refinement ratio of 5, giving an effective resolution of 100 cells per half-reaction zone length (i.e., where half the chemical energy of the reaction has been released) within the reaction zone of the detonation. This high resolution ensures that each reaction step is well resolved (more than 25 cells were present within the zone of each reaction step). All computations are performed with a CFL number of 0.5. The detonation code was initially developed by Mazaheri [30] and extended to a 3-step reaction mechanism for the present study. Details of the numerical methods can be found in Appendix II.

In previous studies using a single step Arrhenius rate law, the stability of the detonation wave is usually characterized by the activation energy of the rate law. As the activation energy increases beyond the value for the stability limit, the detonation front changes from small harmonic oscillations to non-linear pulsations and eventually to chaotic behavior when the activation energy is far from the stability limit value [23]. In fact, the activation energy is a parameter in the single-step rate law that controls the ratio between the induction and reaction zone length, i.e.,

$$\delta = \frac{\Delta_{Induction}}{\Delta_{Reaction}} \tag{2.9}$$

To understand more clearly the nonlinear pulsating instability of the detonation, we should emphasize the importance of the ratio δ. To obtain this ratio δ, the values of the induction zone and reaction zone length are determined from the heat release curve as shown in figure 2.5. The black dot corresponds to the maximum heat release rate or the inflection point of the curve.

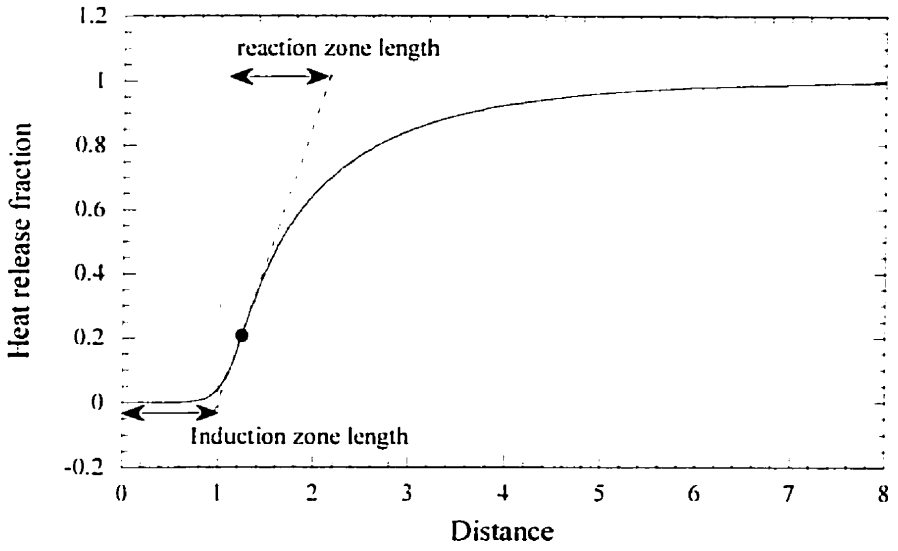

Figure 2.5: Heat release profile using $Q = 10$, $\gamma = 1.2$, $E_I = 20$, $E_B = 8$ and $T_I = 3T_{shock}$ for the 3-step chemical kinetics model.

For the 3-step chemical kinetics model, the ratio between the induction zone and reaction zone length can be changed by varying the chain-branching cross-over temperature T_B, as shown in Section 2.3. Table 2.1 shows the corresponding value of the ratio δ for different chain-branching cross-over temperatures T_B, together with the equivalent activation energy for a single-step rate law. The equivalent activation energy for the single-step Arrhenius rate law is found by matching the inflection point of the heat release curve with the one from the present 3-step chemical kinetics model, such that both chemical kinetics models gives approximately the same ratio between the induction and reaction zone length, as illustrated in figure 2.6. For comparison, the distance is re-normalized with the half-reaction zone length defined as the distance where half the chemical heat has been released.

Chain-branching cross-over temperature T_B	Ratio δ	Equivalent activation energy E_a
0.80 T_{Shock}	0.8975	~13
0.86 T_{Shock}	1.1063	~15
0.88 T_{Shock}	1.1624	~16
0.89 T_{Shock}	1.1989	~16.5
0.90 T_{Shock}	1.2347	~17

Table 2.1: The ratio δ for different chain-branching cross-over temperatures and equivalent activation energies E_a for $Q = 10$, $\gamma = 1.2$, $E_I = 20$, $E_B = 8$ and $T_I = 3T_{shock}$.

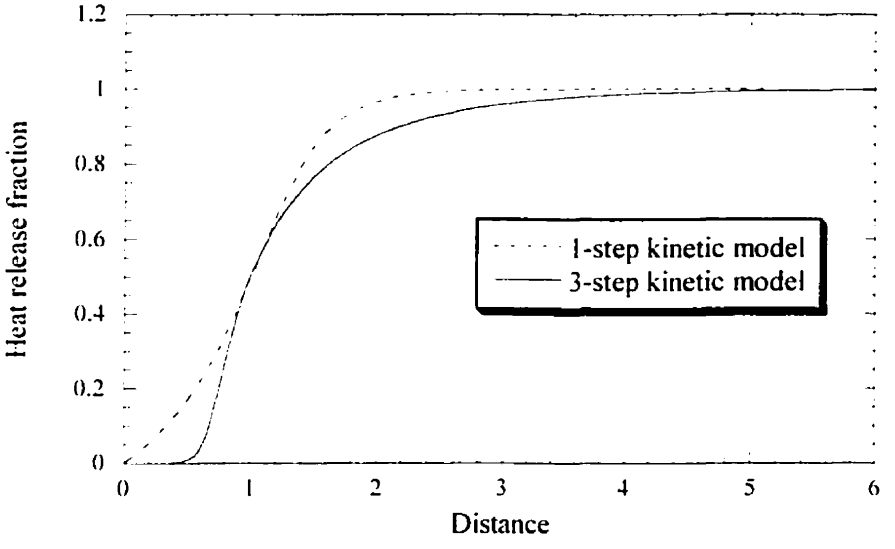

Figure 2.6: Heat release profiles for both the single-step and three-step chemical kinetics models for $Q = 10$ and $\gamma = 1.2$.

The results obtained from the numerical computations using the 3-step chemical kinetics model are now investigated in detail and compared with those obtained from the standard single-step rate law with different activation energies E_a.

2.4.1 Stable detonation with $\delta < 1$

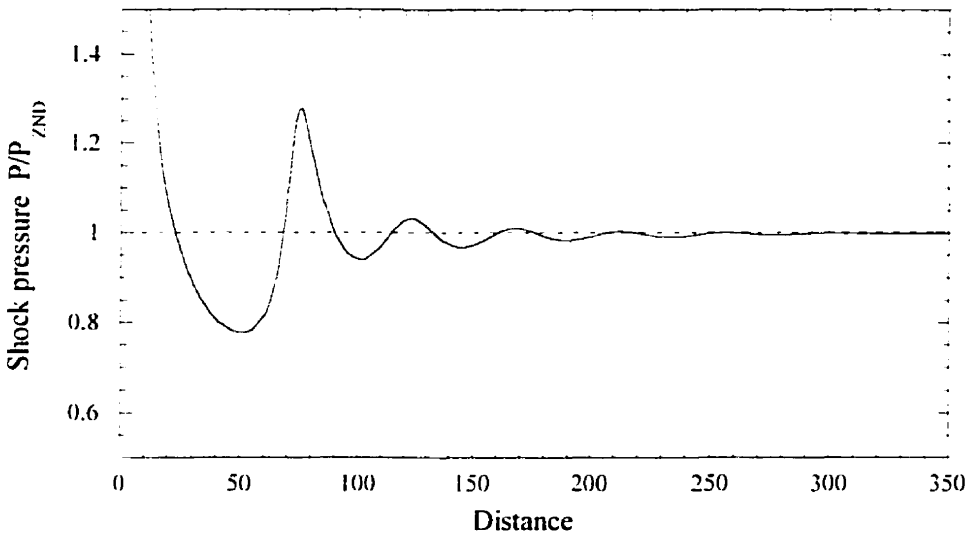

Figure 2.7: Shock pressure history for a stable detonation wave with $T_B = 0.80T_{shock}$ for the three-step chemical kinetics model.

Figure 2.7 shows the pressure history of the shock front for chain-branching cross-over temperature T_B equal to $0.80T_{shock}$ for the 3-step kinetics model. From the steady ZND structure, we know that for $T_B = 0.80T_{shock}$, the induction zone length is short compared to the recombination or reaction zone length. The ratio δ is equal to 0.8975. At the early time, a small amplitude oscillation is observed due to the initiation process. However, after a period of time, the oscillation is damped out and the detonation wave eventually approaches to a stable steady state solution. Comparison between the detonation profiles from steady ZND calculation and transient calculation is given in figure 2.8. It shows that both results are in good agreement. Here, we can see that for small ratio δ (less than 1), the steady detonation wave is stable to small perturbation and a steady ZND solution can be achieved asymptotically.

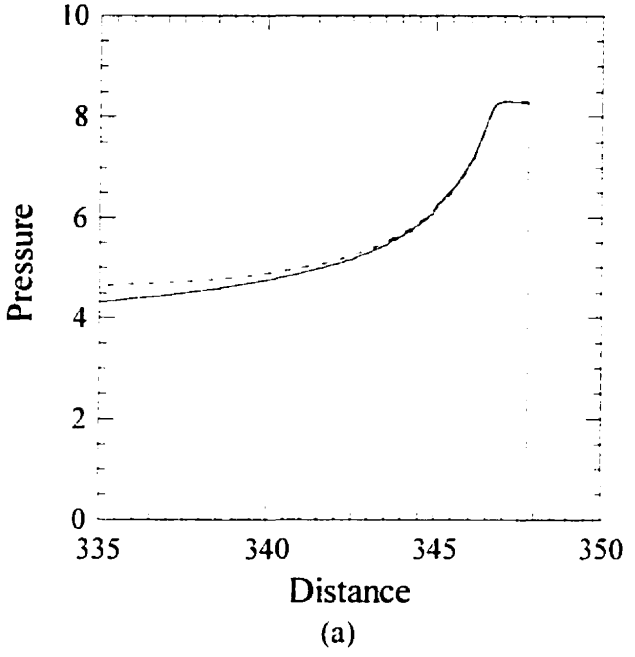

(a)

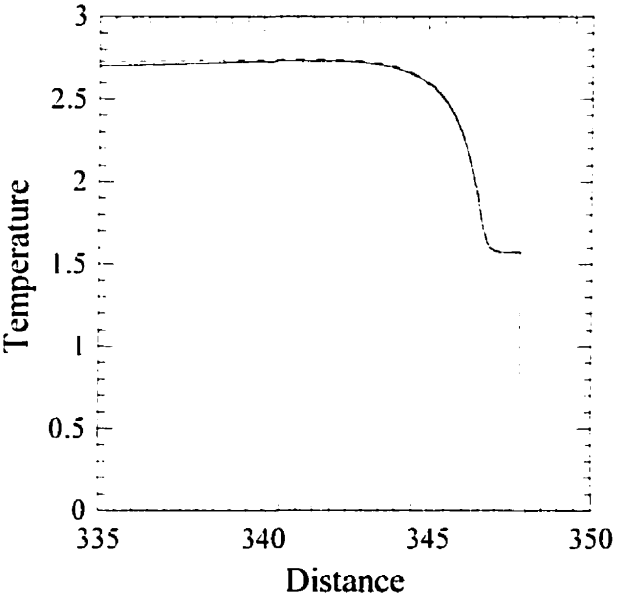

(b)

Figure 2.8: Comparison between the steady ZND solution (dashed lines) and the asymptotic solution from transient calculation (solid lines) for $T_B = 0.80T_{shock}$ for the three-step chemical kinetics model. (a) Pressure profile and (b) temperature profile.

Similar result is also obtained using a single-step rate law with activation energy E_a = 13. This value of activation energy for mixture with Q = 10 and γ = 1.2 also corresponds to a stable detonation, as illustrated in figure 2.9.

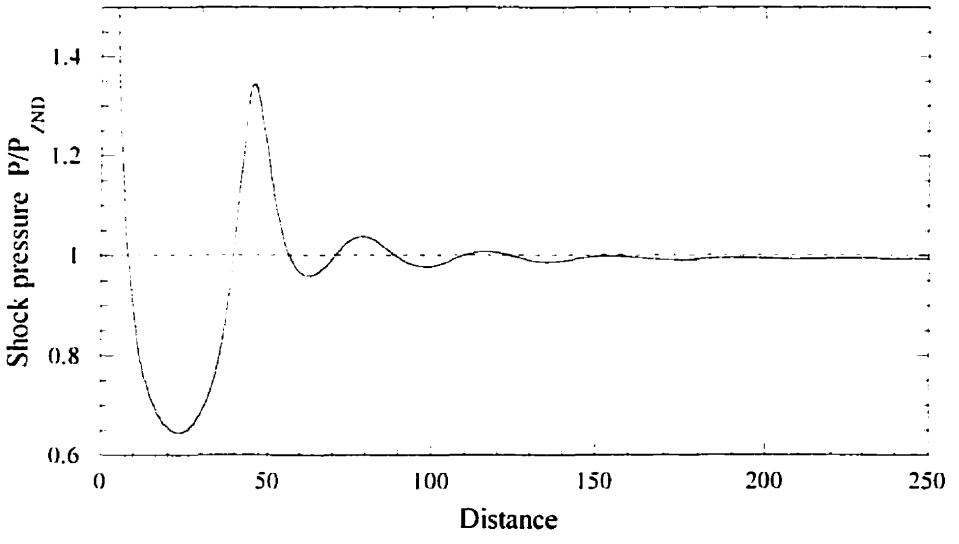

Figure 2.9: Shock pressure history for a stable detonation wave using single-step chemical kinetics model with activation energy E_a = 13.

2.4.2 Unstable detonation with $\delta \approx 1$

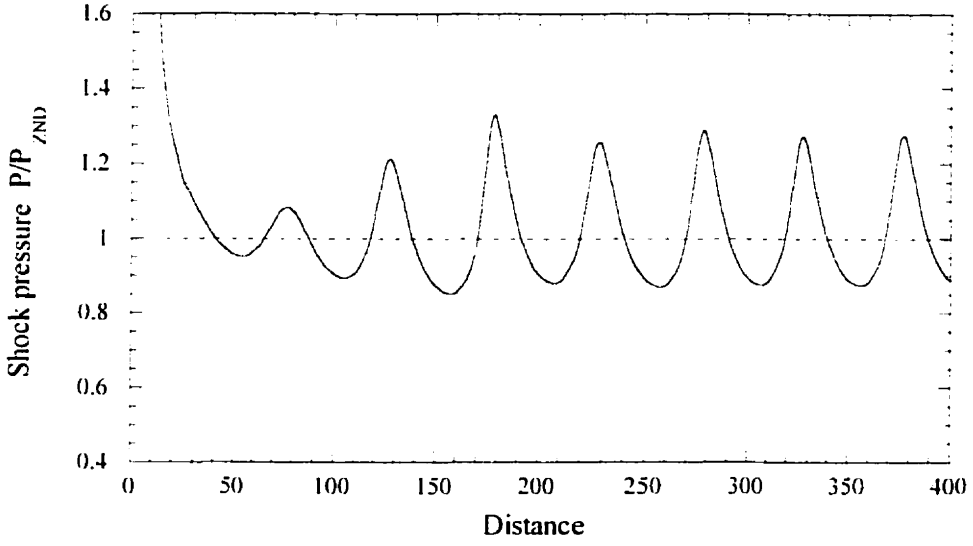

Figure 2.10: Shock pressure history for an unstable detonation wave (a regular harmonic oscillation) with $T_B = 0.86T_{shock}$ for the three-step chemical kinetics model.

By increasing the chain-branching cross-over temperature T_B to $0.86T_{shock}$, thereby increasing the chain-branching induction length relative to the length of the recombination region giving a value of $\delta = 1.1063$, an unstable detonation wave is obtained asymptotically, as shown in figure 2.10. Hence for high value of T_B, a stable detonation cannot be achieved from a transient calculation. For $T_B = 0.86T_{shock}$, the oscillation demonstrates a regular oscillatory behavior with constant period. This phenomenon is generally referred to as a pulsating detonation and it is shown that this occurs when the ratio δ is close to 1. The instability mechanism underlying the steady constant period and frequency pulsation is due to the periodic low-frequency, finite amplitude compression and expansion waves in the chain-branching induction zone between the main reaction region of the reaction zone and the leading shock [37].

Increasing the activation energy for a single-step Arrhenius rate model has the same effect as increasing the induction length relative to the reaction length. Figure 2.11 shows the pressure history of the shock front for activation energy E_a

= 15 using the single step Arrhenius rate law. Similar pulsating phenomenon with a regular harmonic oscillation is observed.

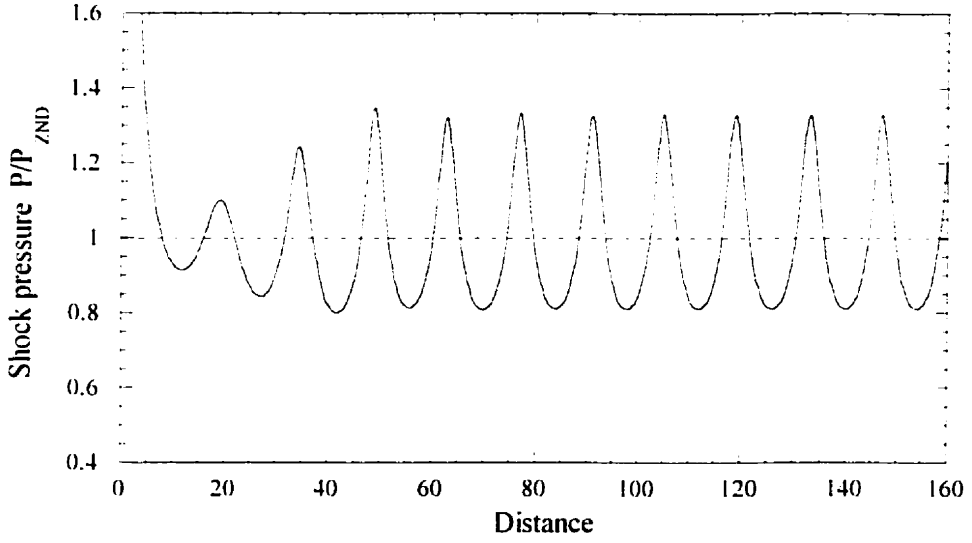

Figure 2.11: Shock pressure history for an unstable detonation wave (a regular harmonic oscillation) using single-step chemical kinetics model with activation energy $E_a = 15$.

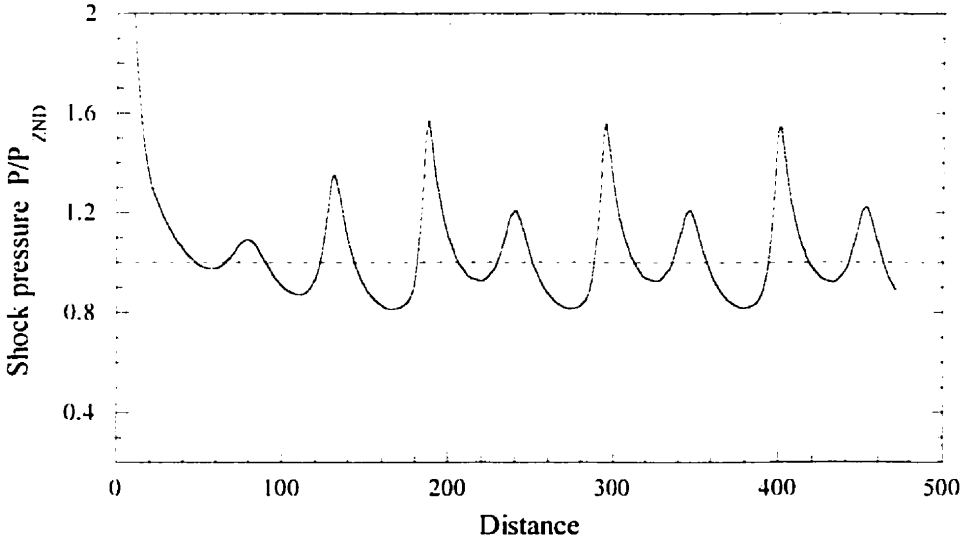

Figure 2.12: Shock pressure history for an unstable detonation wave (a period-doubling bifurcation mode) with $T_B = 0.88T_{shock}$ for the three-step chemical kinetics model.

Further increase in the chain-branching cross-over temperature T_B for the three-step kinetics model causes the oscillation to become less regular. The ratio δ eventually becomes bigger than 1. For $T_B = 0.88T_{shock}$, a bifurcation occurs. A steady period-doubled oscillation can be observed, as illustrated in figure 2.12. It consists of a high amplitude oscillation followed by a smaller-amplitude oscillation. A bifurcation mode of oscillation is also observed for activation energy $E_a = 16$ for the computation using the single-step Arrhenius rate law, as shown in figure 2.13.

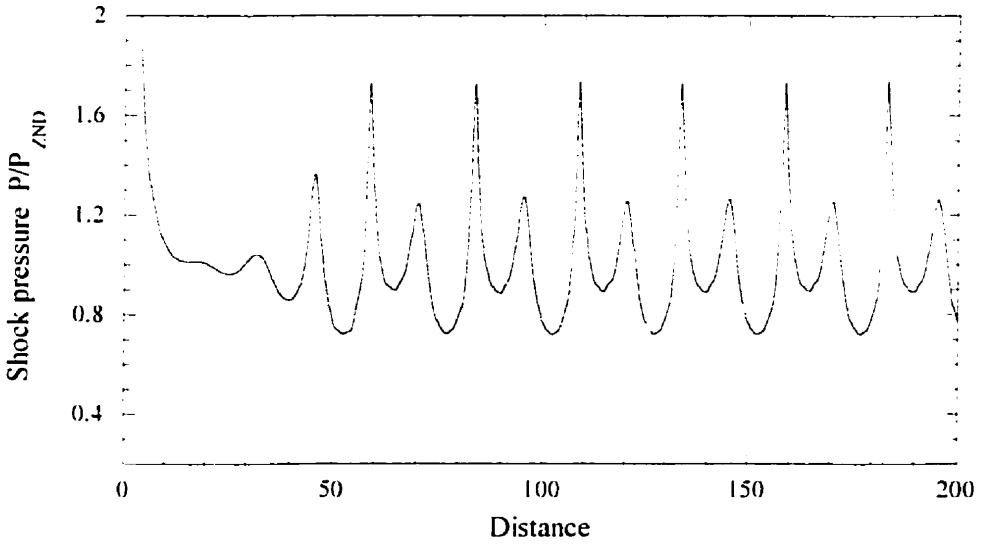

Figure 2.13: Shock pressure history for an unstable detonation wave (a period-doubling bifurcation mode) using single-step chemical kinetics model with activation energy $E_a = 16$.

2.4.3 Highly unstable detonation with δ>1

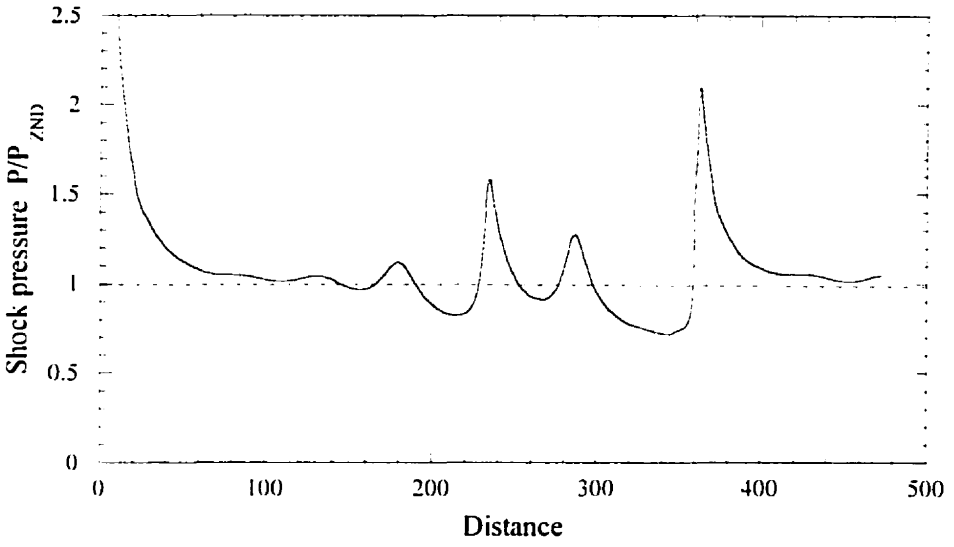

Figure 2.14: Shock pressure history for an unstable detonation wave (a chaotic oscillation mode) with $T_B = 0.89T_{shock}$ for the three-step chemical kinetics model.

For a very large value of T_B, a very long chain-branching induction zone occurs which can significantly affect the propagation of detonation waves. A highly non-steady behavior with a number of oscillations of different amplitudes and periods is observed, as shown in figure 2.14. This result shows that no steady solution can be obtained. The oscillation is chaotic and is generally called a multi-mode pulsating detonation. In this case, the instability mechanism is more complex because a secondary detonation is formed behind the lead detonation shock and thus leads to a shock-shock interaction. This accounts for the observation of the highly irregular behavior. We can obtain the same phenomenon by increasing the activation energy for the single step kinetics model to $E_a = 16.5$ (figure 2.15).

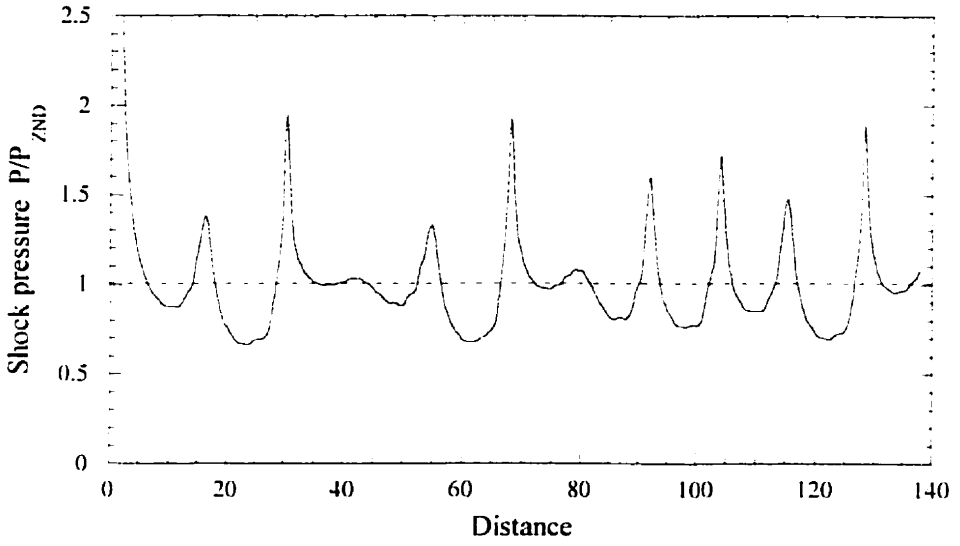

Figure 2.15: Shock pressure history for an unstable detonation wave (a chaotic oscillation mode) using single-step chemical kinetics model with activation energy $E_a = 16.5$.

2.4.4 Detonability limit

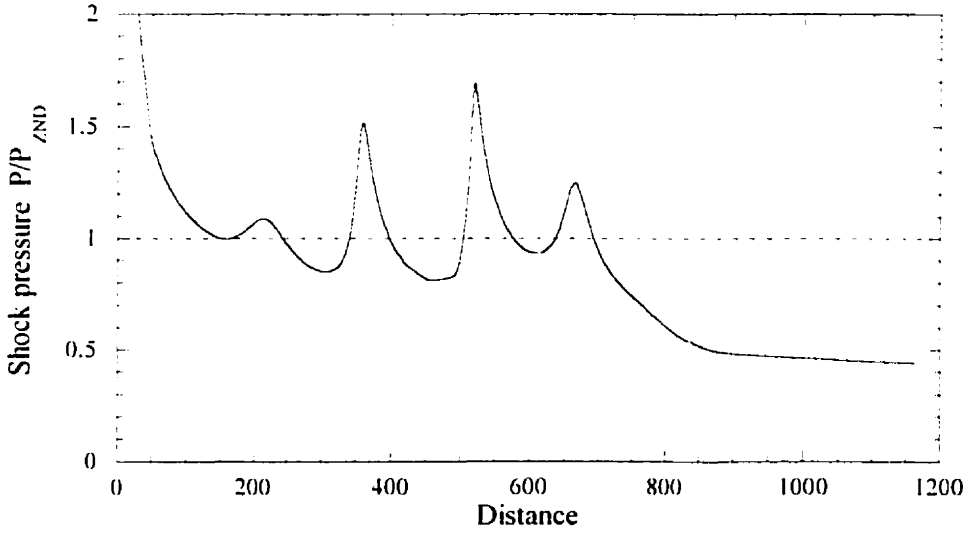

Figure 2.16: Quenching of detonation wave: detonability limit with $T_B = 0.90T_{shock}$ for the three-step chemical kinetics model.

If T_B continues to increase further, then at some value T_B (i.e., T_B = $0.90T_{shock}$ giving a ratio δ = 1.2347), the detonation wave fails. This phenomenon is demonstrated in figure 2.16. For sufficiently large T_B, the reaction zone (where the chemical energy is released) is at a distance far away from the shock front. With a large amplitude fluctuation, the shock temperature will drop below the chain-branching cross-over temperature T_B. The rate constant for the chain-branching reaction is very small and has a profound effect on the rate of radical production behind the shock. The chain-branching reaction can be considered to be "switched off". Decoupling between the detonation shock and reaction zone occurs. The energy released from the reaction zone cannot sustain the detonation wave and eventually the detonation wave quenches.

For the numerical result using a single-step kinetics rate law, He & Lee [23] found that the dynamic quenching phenomenon occurs only at very high value of activation energy (far above E_a = 17 in this case). They argue that there exists a dynamic limit of activation energy for which the detonation cannot propagate via auto-ignition mechanism. However, Sharpe & Falle [35] recently found that even at high value of activation energy for the one-step Arrhenius rate law, the detonation wave still propagates as a series of explosion if one uses a very refined numerical grid for the computation. Therefore, for single-step chemistry, there is no clear definition for this detonation limit. Unlike a detonation wave using a one-step Arrhenius chemical reaction, a clearer criterion for the failure can now be established using the present three-step kinetics model. Short & Quirk in their paper state that:

> *"If the detonation shock temperature drops to the chain-branching cross-over temperature T_B, the detonability limit occurs." [36]*

In the present study, the resulting solutions from transient initial developments are very similar to those obtained from a non-linear stability analysis of the ZND solution by Short & Quirk. It is demonstrated that the pulsating behaviour found for the present three-step reaction model is also similar to the pulsating detonation

instabilities found for the standard one-step reaction model [36]. The difference is that the present kinetics model possesses a well-defined detonability limit. The chemical switch-off mechanism found in this three-step reaction model that causes the quenching to occur is not present for one-step Arrhenius reaction kinetics.

From the present result using two different chemical kinetics models, we can suggest that the ratio between the induction zone and reaction zone length is the main parameter (independent of the rate process), which characterizes the stability of detonation wave. The significances of these two length scales on the detonation stability have been first discussed by Short & Quirk [36] and also experimentally observed by Borisov *et al.* [6]. In the present study, we see that if the value δ is much smaller than 1, where the reaction zone length is always larger than the induction zone length, the detonation wave is stable. When the value δ approaches to 1, the detonation wave starts to become weakly unstable. This implies that as soon as the induction stage of the reaction becomes dominant, the wave becomes unstable to perturbation. Slightly above 1, regular oscillation of the detonation front can be observed. If this ratio is much larger than 1, the shock front oscillates in a chaotic manner and eventually detonability limit occurs due to the high instability of the detonation.

Since this ratio offers a reasonable explanation of some marginal features of detonations, thus in the following chapter, this ratio will be used to characterize the mixture for simplicity.

Chapter 3

Direct Initiation of Detonation

3.1 Introduction

In this Chapter, the phenomenon of direct initiation is investigated for the planar, cylindrical and spherical geometries using a more realistic chemical kinetic model than the single-step Arrhenius rate model used in almost all of the previous investigations. We shall adopt the ideal strong blast wave model as initial condition in the present simulation of direct initiation phenomenon.

For ideal strong blast waves, the initial condition used in the numerical simulations is given by the similarity solution for non-reacting blast wave of Taylor and Sedov [33, 38]. The subsequent decay of the blast, when chemical reaction comes into play, has to be described by the numerical integration of the reactive Euler equations with the appropriate chemical rate law. The similarity solution for non-reacting strong blast waves gives the following relationship between the strength of the shock M_s, the shock radius R_s and the source energy E_s, i.e.,

$$\frac{E_s}{P_o} = \alpha_j \left(\frac{j+3}{2} \right)^2 \gamma M_s^2 R_s^{j+1} \tag{3.1}$$

where α_j is a constant obtained from blast wave theory ($\alpha_0 = 2.257$, $\alpha_1 = 2.026$, $\alpha_2 = 1.739$), which is a function of the adiabatic exponent γ. P_o is the initial pressure of the mixture and j is the geometric index, i.e., $j = 0, 1, 2$ for the planar, cylindrical and spherical geometries, respectively. Knowing the initial shock strength and location, the initiation energy can be determined from this relationship. Equation 3.1 will be used for all the following computations to obtain the initiation energy for direct initiation.

3.2 The three regimes of direct initiation

From the experimental investigation of direct initiation of spherical detonation of Bach *et al.* [3], we know that the initiation process can be classified into three regimes, i.e., subcritical, supercritical and critical regimes according to whether the source energy is less than, greater than, or equal to a threshold value corresponding to the critical energy. The three regimes of direct initiation are first simulated for planar geometry and their mechanism is discussed in this section. A mixture that corresponds to stable detonation is first investigated.

3.2.1 The subcritical regime

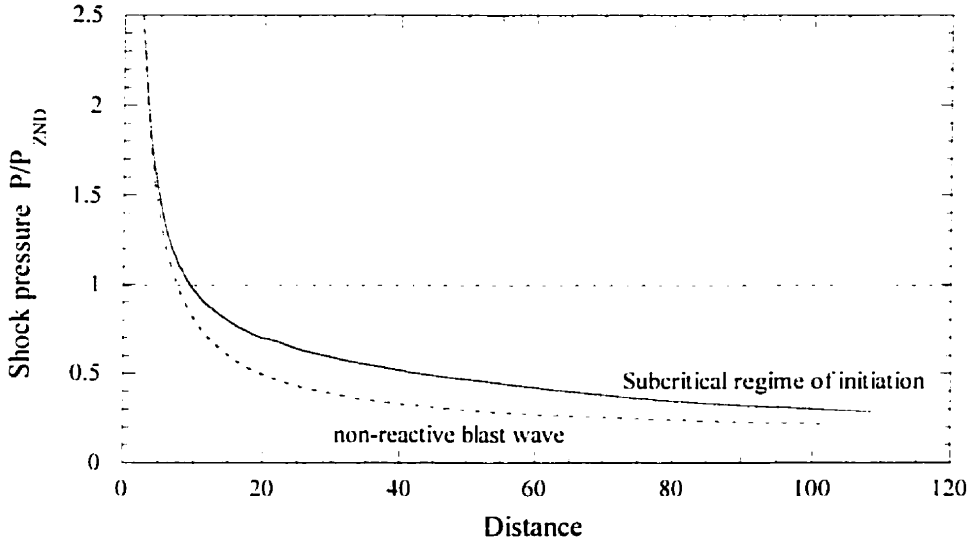

Figure 3.1: Shock pressure history for the subcritical regime of initiation for Q = 10. γ = 1.2 and δ = 0.5652 (The dashed lines represent the non-reactive blast wave) with non-dimensional initiation energy E_s = 342.

Upon the sudden deposition of a large amount of energy in a gaseous combustible mixture, a strong blast wave is formed. During the early times of the blast wave propagation, the shock pressure decreases rapidly as in a strong non-

reactive blast wave since the blast energy dominates the decay process. As the blast decays to larger distances, the chemical heat release starts to influence the blast wave propagation (at about $M_s < 1.5M_{CJ}$). If the source energy is far below the critical value, the chemical reaction zone will fail to couple to the shock front and the blast continues to decay to sonic speed asymptotically. This initiation phenomenon is referred to the subcritical regime of initiation where the source energy is below the critical value. Figure 3.1 shows the shock pressure history for the subcritical regime of initiation, together with that of a non-reactive blast wave for comparison. In this case, the non-dimensional initiation energy E_s (i.e., E_s/P_o) is equal to 342. As the blast wave continues to decay, the combustion front will recede further from the shock front. The shock progressively decays to sonic velocities, similar to the non-reactive blast wave propagation, while the combustion zone propagates as a slow deflagration wave.

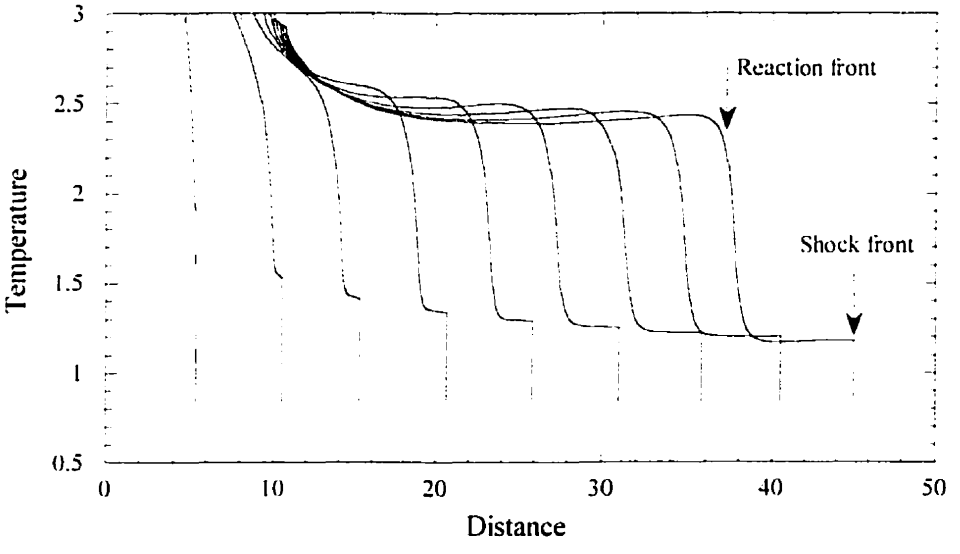

Figure 3.2: Temperature profiles at different times for the subcritical regime of initiation for $Q = 10$, $\gamma = 1.2$ and $\delta = 0.5652$ with non-dimensional initiation energy $E_s = 342$.

The decoupling between the reaction front and the leading shock can be clearly observed from the temperature profiles. Figure 3.2 shows the temperature profiles at different times during the blast decay. In the subcritical regime, two

sharp temperature rises can be seen in the profiles. The first abrupt rise in the temperature is due to the adiabatic shock compression. A short plateau follows where the temperature remains almost constant. This distance corresponds to the induction zone length, i.e., the region where the "incubation" process takes place and the reactants start to dissociate into free radicals. After the induction period, the chemical energy release starts because the recombination process of radicals is exothermic. Thus, a second rise in temperature occurs due to the rapid chemical heat release. This second jump in temperature can be defined as the reaction front. In the early times of blast wave propagation, the induction zone is extremely short (almost not perceptible) due to the high temperatures. Thus, the two fronts are coupled and can hardly be distinguished from each other. However, as the blast decays to weaker strength, the shock temperature is lower and the induction time increases. The shock and the reaction front then start to decouple as the induction length increases.

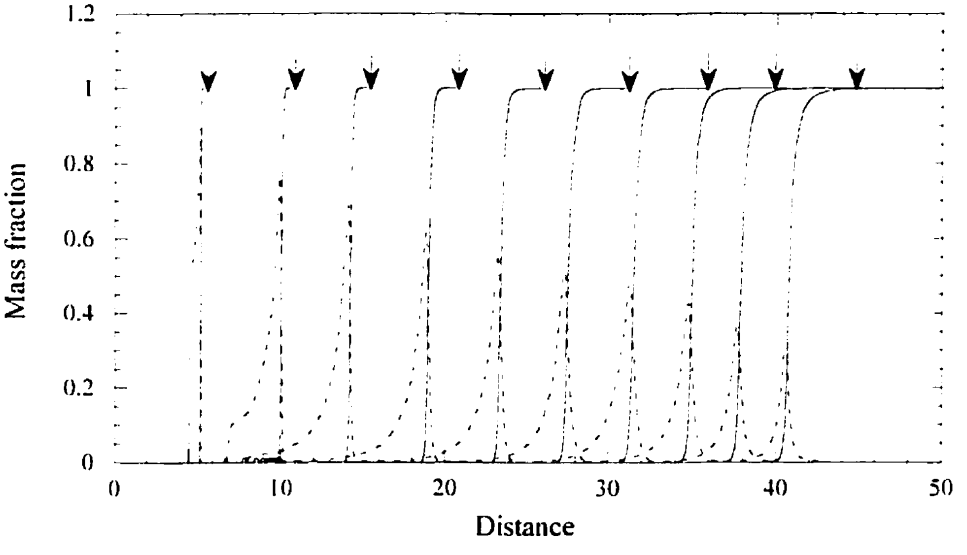

Figure 3.3: Detonation structure profiles showing the mass fraction of fuel (solid lines) and radical (dashed lines) for the subcritical regime of initiation for $Q = 10$, $\gamma = 1.2$ and $\delta = 0.5652$ with non-dimensional initiation energy $E_s = 342$. The arrows indicate the leading shock front.

The reason for the decoupling phenomenon can be explained by looking at the profiles showing the mass fraction of fuel and radicals (figure 3.3). At the early decay of the blast, the chain-branching induction zone is small and there is a significant buildup of chain radical concentration at the combustion front. As the blast expands further, the rate of the chain-branching reaction decreases, resulting in a lower peak concentration of chain radicals. Once the temperature drops below the chain-branching cross-over temperature T_B, the chain-branching reaction step is essentially "switched off" and no further radical buildup can be observed in the reaction zone. This leads to a significant increase in the induction zone length and results in a decoupling of the combustion front and the leading shock.

3.2.2 The supercritical regime

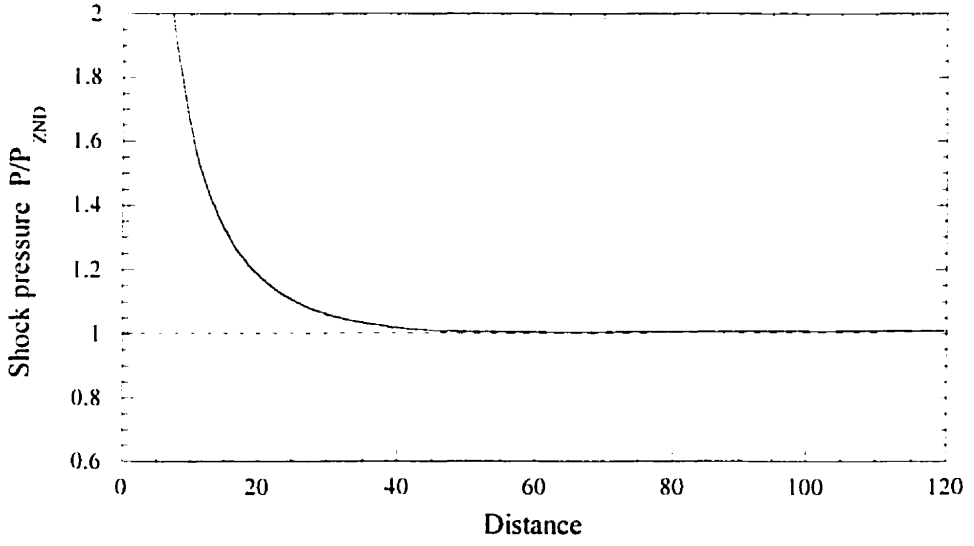

Figure 3.4: Shock pressure history for the supercritical regime of initiation for $Q = 10$, $\gamma = 1.2$ and $\delta = 0.5652$ with non-dimensional initiation energy $E_s = 670$.

If the blast wave generated by the source is of sufficient duration, rapid auto-ignition takes place behind the blast wave and the chemical reaction zone is then intimately couple with the shock. The blast wave decays asymptotically to a

self-sustained C-J detonation. The detonation front will continue to propagate steadily at the C-J velocity thereafter. This corresponds to the so-called supercritical regime of initiation. For this supercritical case, the initiation energy deposited is above the critical value, the flow field simply consists of a continuous decaying blast wave to the C-J velocity of the mixture. The supercritical regime is illustrated in figure 3.4, which shows the pressure history of the shock front for the supercritical regime of initiation. This simulation for supercritical regime of initiation is performed with a non-dimensional initiation energy $E_s = 670$.

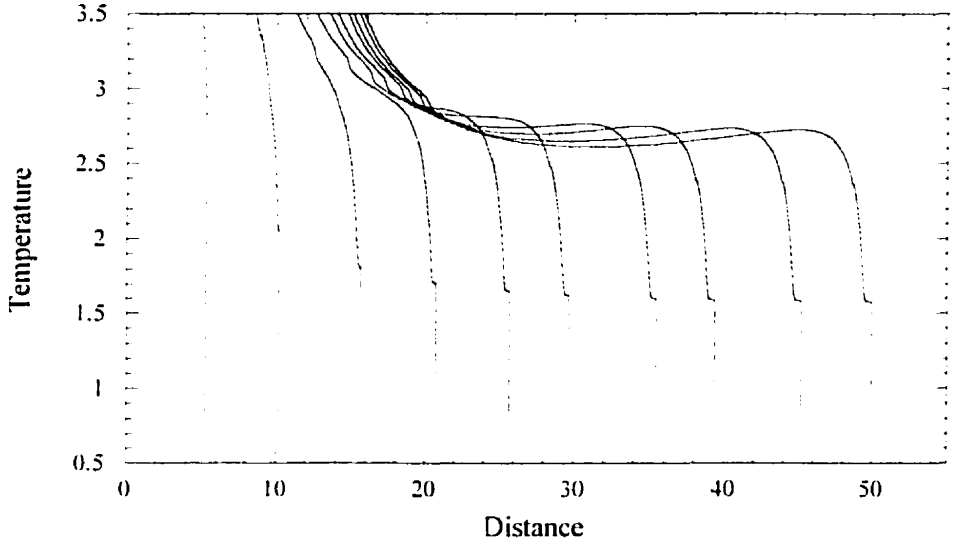

Figure 3.5: Temperature profiles at different times for the supercritical regime of initiation for $Q = 10$, $\gamma = 1.2$ and $\delta = 0.5652$ with non-dimensional initiation energy $E_s = 670$.

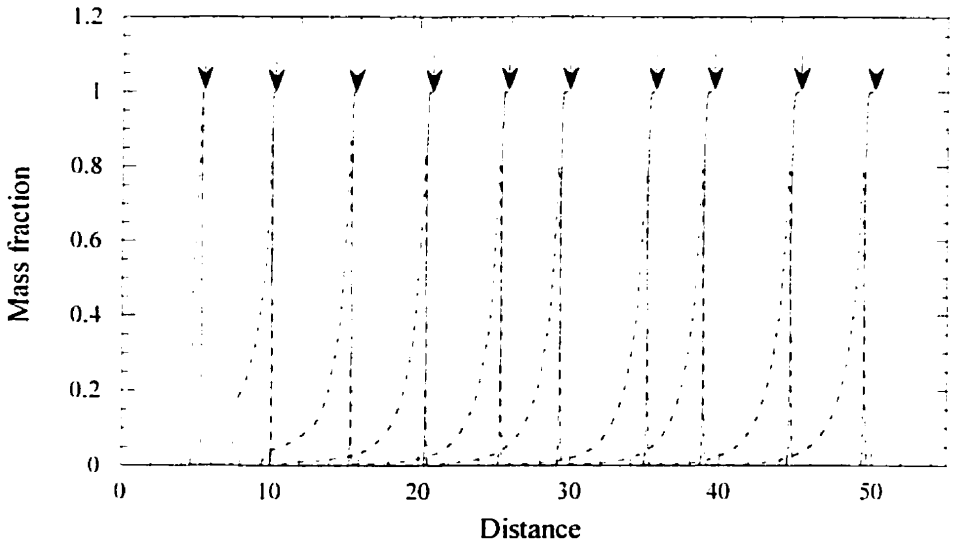

Figure 3.6: Detonation structure profiles showing the mass fraction of fuel (solid lines) and radical (dashed lines) for the supercritical regime of initiation for $Q = 10$, $\gamma = 1.2$ and $\delta = 0.5652$ with non-dimensional initiation energy $E_s = 670$. The arrows indicate the leading shock front.

Figure 3.5 shows the temperature profiles. From this figure, we note that the temperature rise due to the heat release by combustion almost coincides with the temperature rise due to shock front compression. This indicates that the combustion front is intimately coupled to the shock front throughout. Also, from the mass fraction of fuel and radicals profiles (figure 3.6), we note that there is always a significant amount of chain radicals in the reaction front.

3.2.3 The critical regime

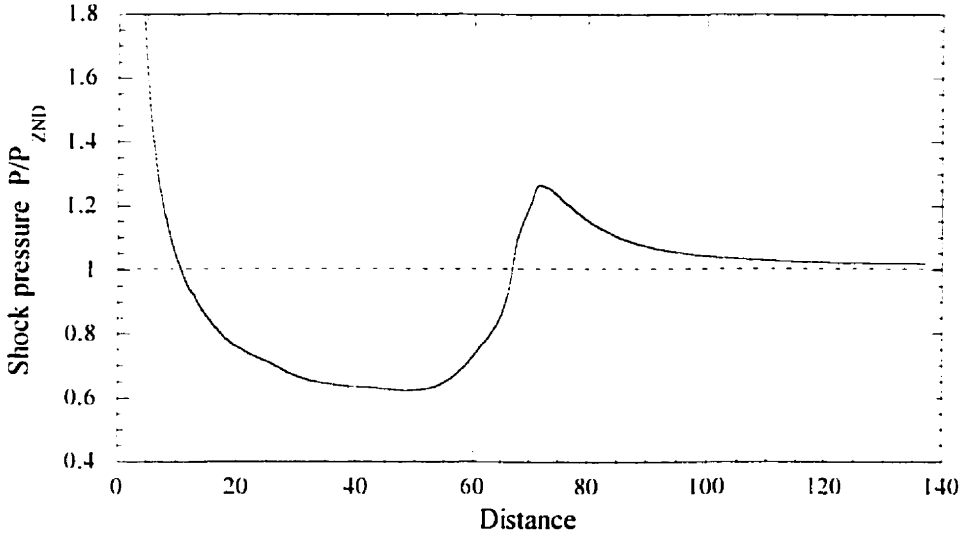

Figure 3.7: Shock pressure history for the critical regime of initiation for $Q = 10$, $\gamma = 1.2$ and $\delta = 0.5652$ with non-dimensional initiation energy $E_s = 370$.

If the initiation energy is near the critical value, the phenomenon is more complex as illustrated in figure 3.7. Here, the non-dimensional initiation energy E_s has a value of 370. When the initiation energy near the critical value, the shock front and the reaction front decouple as the blast expands. The reaction front recedes from the leading shock. However, unlike the subcritical case, where the reaction zone continually recedes from the shock, the decoupling in the critical case stops after the blast has decayed to a certain shock velocity. Thereafter both the shock and the reaction front propagate together as a quasi-steady complex at a Mach number near the auto-ignition limit of the mixture. This is referred to as the quasi-steady period and this quasi-steady period terminates when the shock front abruptly re-accelerates to an overdriven detonation wave. The overdriven wave eventually decays to a self-sustained detonation wave. If the initiation energy is smaller than this critical value, the decoupling will continue and the shock will eventually decays to an acoustic wave ($M_s = 1$) and no detonation is initiated, as in the subcritical case.

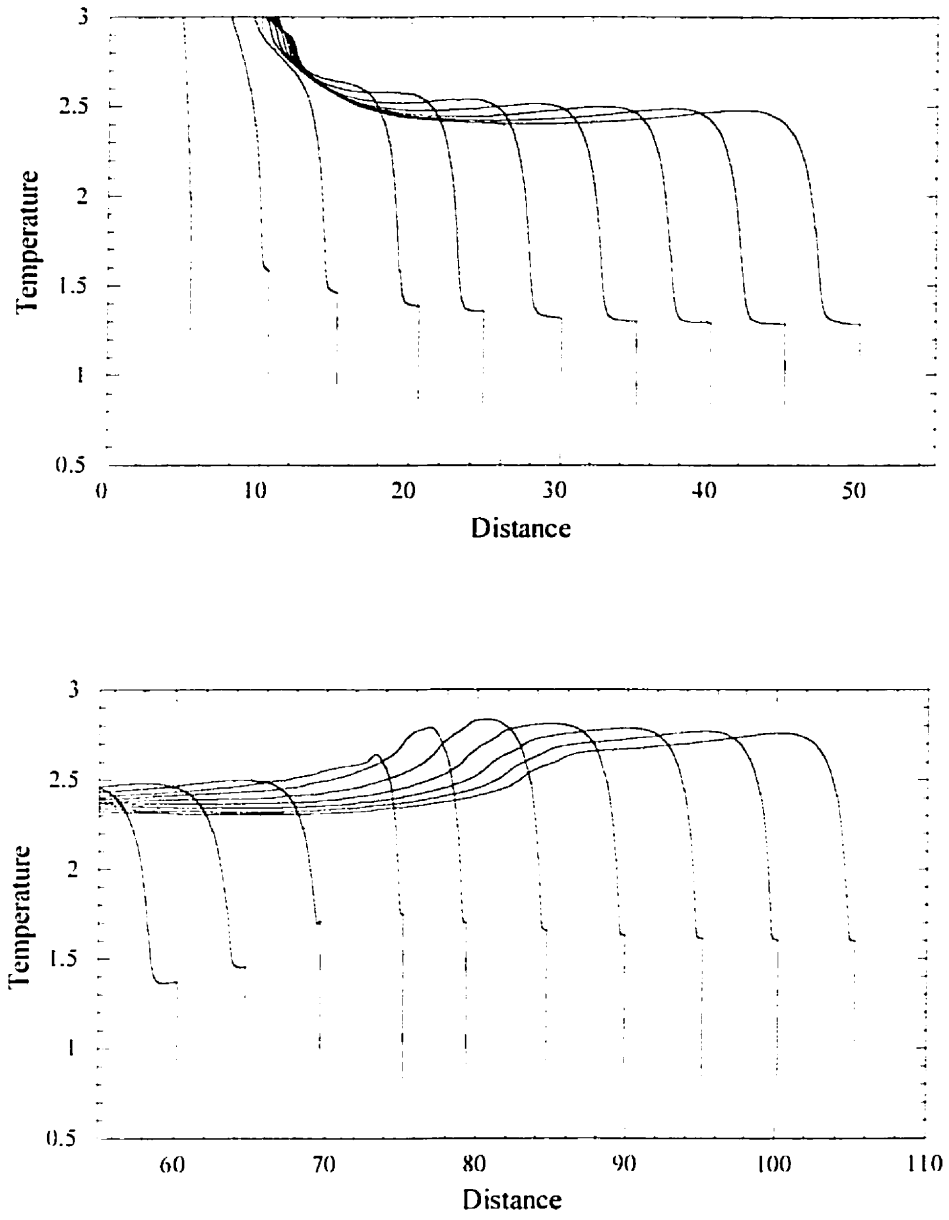

Figure 3.8: Temperature profiles at different times for the critical regime of initiation for $Q = 10$, $\gamma = 1.2$ and $\delta = 0.5652$ with non-dimensional initiation energy $E_s = 370$.

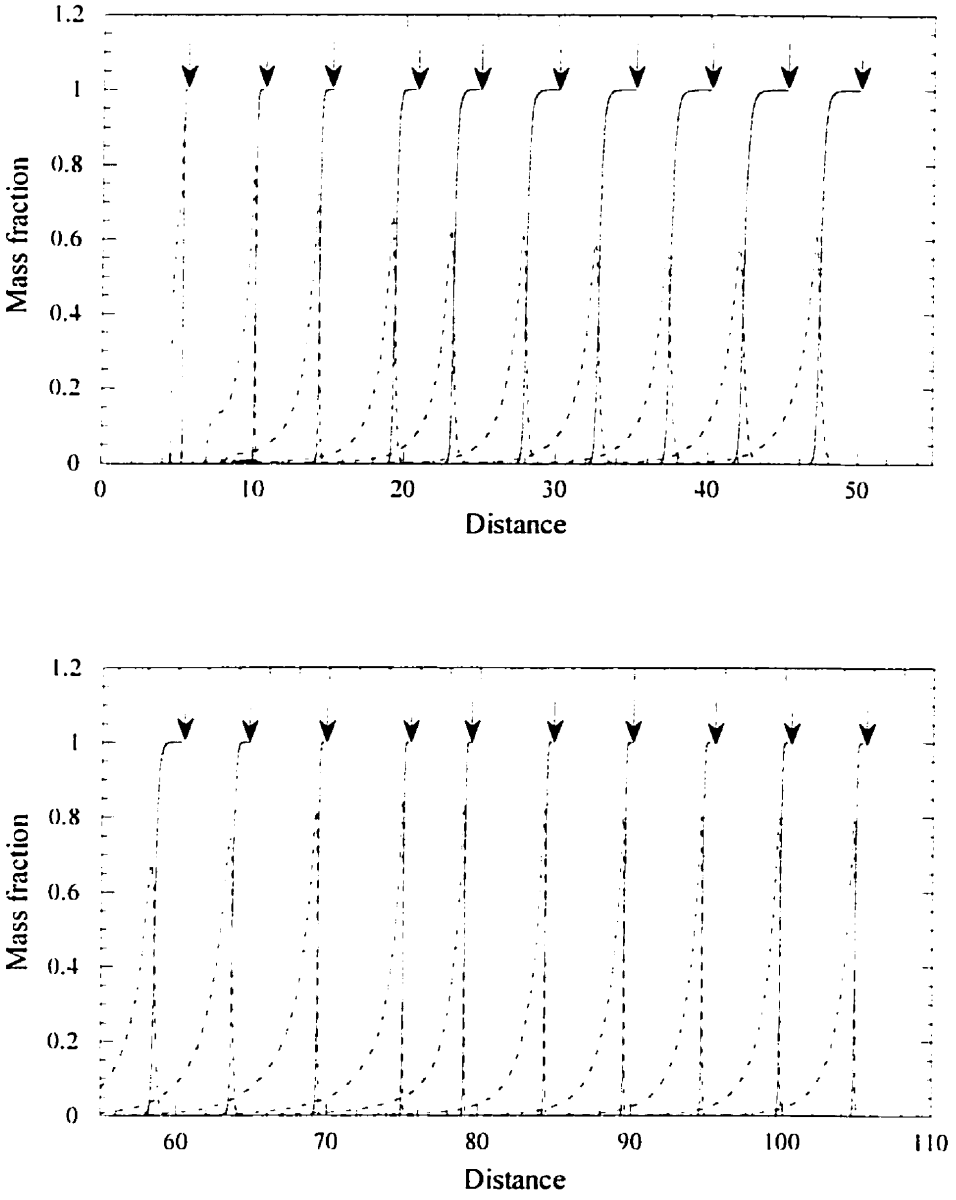

Figure 3.9: Detonation structure profiles showing the mass fraction of fuel (solid lines) and radical (dashed lines) for the critical regime of initiation for Q = 10, γ = 1.2 and δ = 0.5652 with non-dimensional initiation energy E_s = 370. The arrows indicate the leading shock front.

Figure 3.8 shows the temperature profiles at different times for the critical regime of initiation. During the early blast decay, the distance between two fronts progressively increases as the two fronts decouple from each other. Near the end

of the quasi-steady period, the distance between two fronts decreases again and the shock begins to accelerate and finally two fronts become completely coupled. The shock temperature at the quasi-steady regime is found to correspond closely to the chain-branching cross-over temperature T_B. Same phenomenon can be observed in Figure 3.9 showing the mass fraction of reactants and radicals during the initiation process.

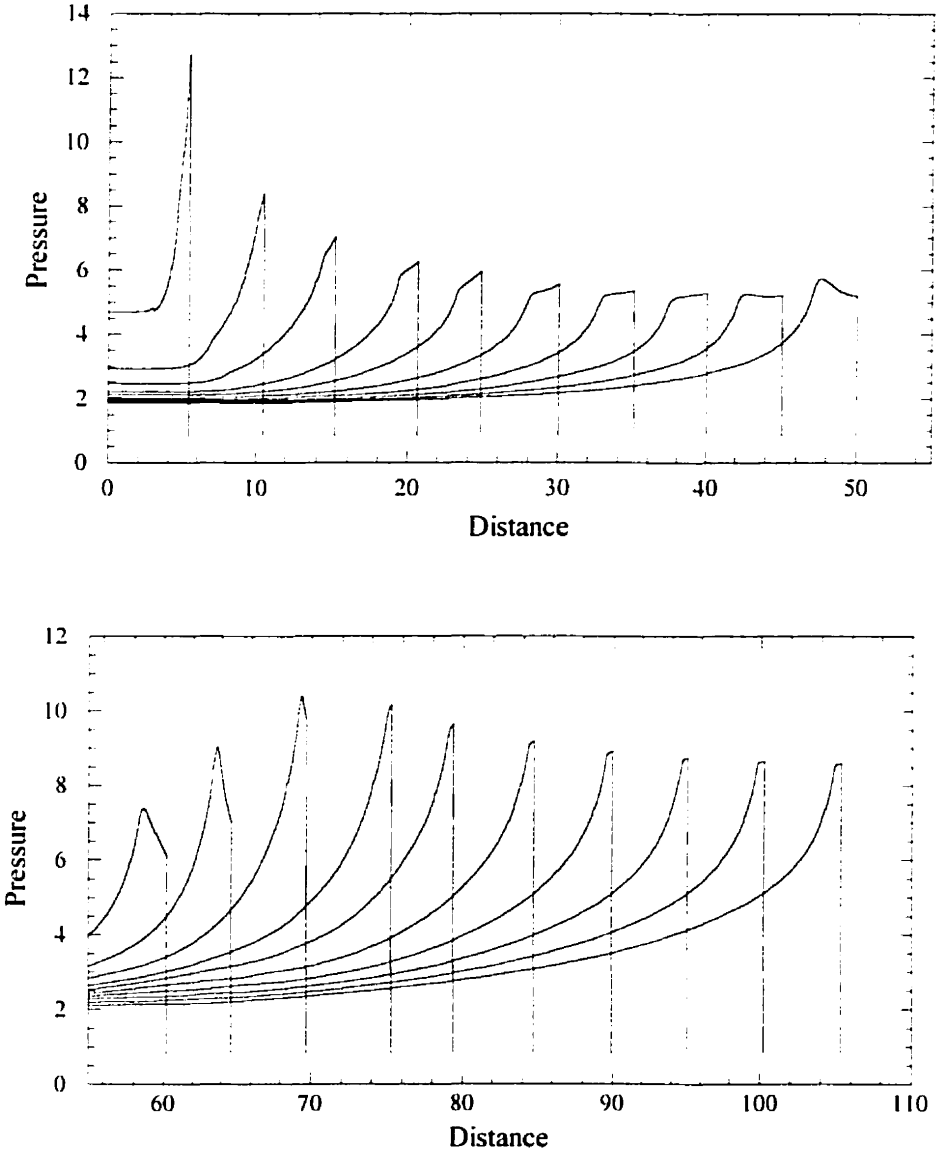

Figure 3.10: Pressure profiles at different times for the critical regime of initiation for $Q = 10$, $\gamma = 1.2$ and $\delta = 0.5652$ with non-dimensional initiation energy $E_s = 370$.

To understand the re-acceleration process before the onset of detonation, some observations can be made from the analysis of the pressure profiles. Figure 3.10 shows the pressure profiles for the critical regime of initiation. At the early decay, the shock pressure and the pressure gradient at the shock are decreasing as the shock moves forward. A pressure pulse begins to develop in the region between the reaction front and the leading shock. As the reaction-shock complex moves, this pressure pulse starts to amplify. This pressure pulse eventually becomes the maximum pressure in the flow field. The distance between the reaction front and the peak pressure decreases as the structure moves. As the strength of the pressure pulse increases, the shock front accelerates because the high pressure region begins to drive the shock front. The leading shock and the reaction front eventually merge together to form an overdriven detonation. The mutual interaction of the pressure pulse and the chemical heat release results in the rapid amplification of the pressure pulse and the onset of a detonation. This is the essence of the mechanism of shock wave amplification by coherent energy release (SWACER), first proposed by Lee [28]. The re-establishment of the front in the critical regime of initiation is due to the generation and amplification of a pressure pulse between the leading shock and combustion front. This process of rapid shock amplification at the end of the quasi-steady period can be explained by the fact that the chemical energy release in the reaction front is synchronized with the propagation of the pressure pulse within the reaction-shock complex.

3.3 SWACER mechanism

It is important to investigate in more detail the mechanism of detonation formation in the critical regime of initiation. During the quasi-steady phase of the critical regime of initiation, the shock amplification at the end of the quasi-steady period is due to synchronization of the chemical energy release with the propagation of the pressure pulse generated within the reaction-shock complex. This concept of shock wave amplification by coherent energy release (SWACER) mechanism was first proposed by Lee *et al.* [28] in the study of photo-chemical

initiation of detonation. The shock wave amplification is basically a phenomenon that involves the phase synchronization between pressure waves and heat release of chemical reactions. To illustrate the idea of SWACER mechanism, consider the example of a moving energy source in a tube. This theoretical model has been first considered by Thibault *et al.* [28]. A planar energy source is assumed to move at a constant velocity V_o depositing a total energy per unit mass Q_o at a rate $w(t)$ such that the rate of energy release $\dot{q}(x,t)$ is given by:

$$\dot{q}(x,t) = w\left(t - \frac{x}{V_o}\right) \cdot H\left(t - \frac{x}{V_o}\right) \tag{3.2}$$

where H is the step function ($H(\tau)=0$ for $\tau<0$ and $H(\tau)=1$ for $\tau>0$). The function $w(t)$ is chosen to have the following form:

$$w(t) = \frac{Q_o t}{\tau_R^2} \exp\left(\frac{-t^2}{2\tau_R^2}\right) \tag{3.3}$$

This heat release function is plotted in figure 3.11. τ_R is the time required for $w(t)$ to reach its peak value. Through this ignition process of moving ignition source, the energy is released in a constant sequence corresponding to a constant induction time. The induction time can be changed using different velocities of the igniter. The development of shock wave due to this traveling energy source was then computed from the non-linear gas-dynamic equations. Details of this theoretical model can be found in ref. [41].

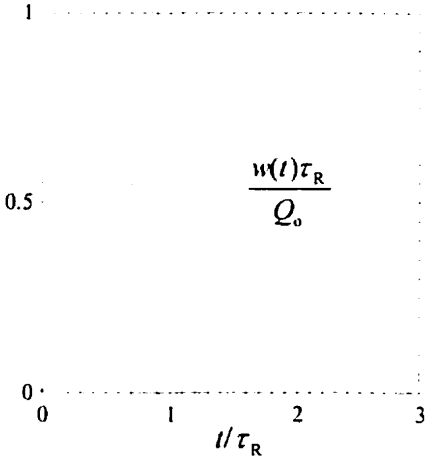

Figure 3.11: Heat release profile for equation 3.2.

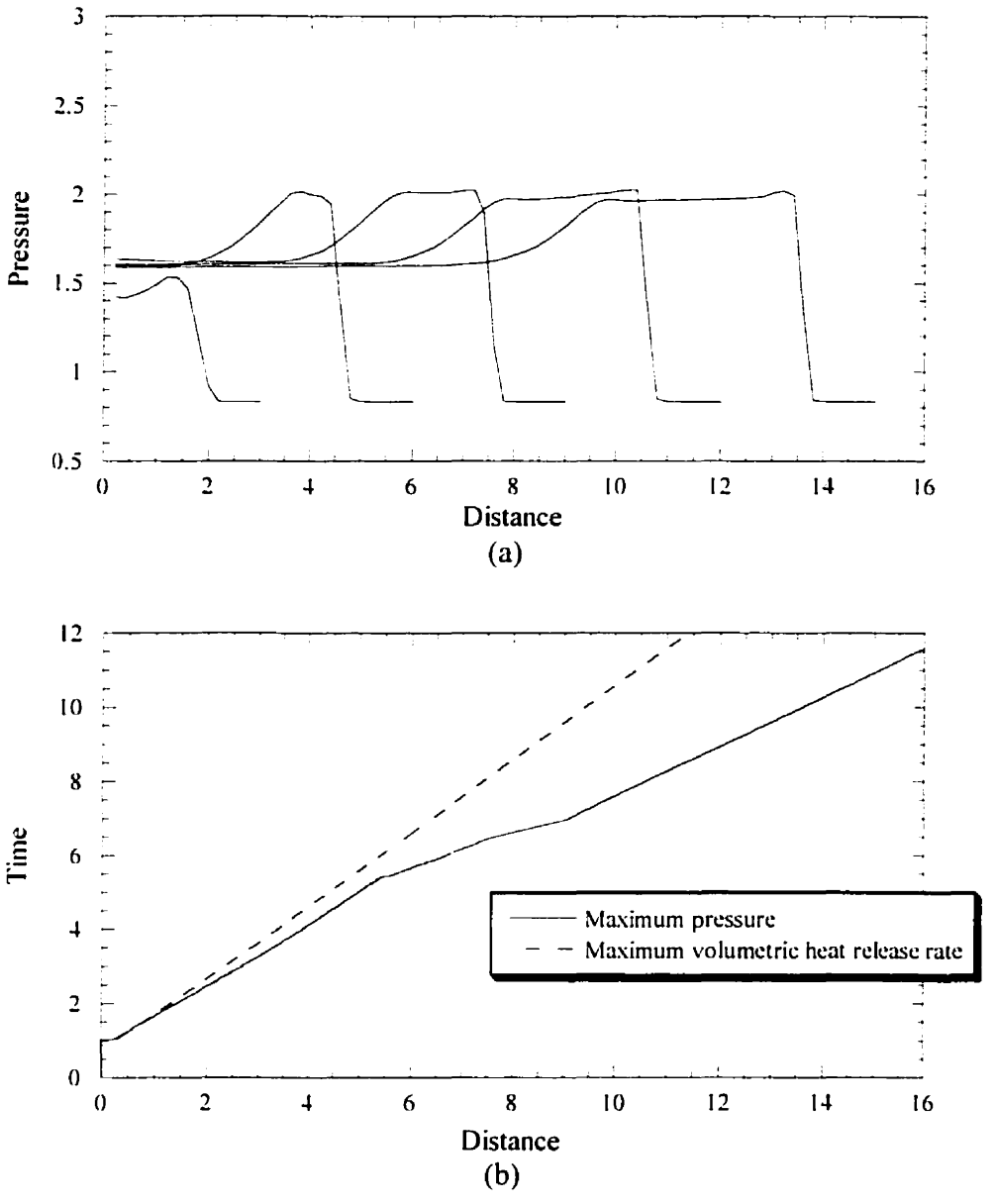

Figure 3.12: (a) Pressure profiles and (b) x-t diagram for M_{source} = 1.

Results obtained for different energy source velocities M_{source} (= V_o/c_o) are now discussed. Figure 3.12 shows the pressure profile and the trajectories of the point of the maximum volumetric energy release rate $(\rho\dot{q})_{max}$ and the maximum pressure point $(P)_{max}$ for the energy source moving at M_{source} = 1. From the x-t diagram (figure 3.12b), we can observe that the early formation of the

compression wave immediately runs away from the energy source. The pressure profile shows that only a weak amplification of the pressure pulse can be obtained.

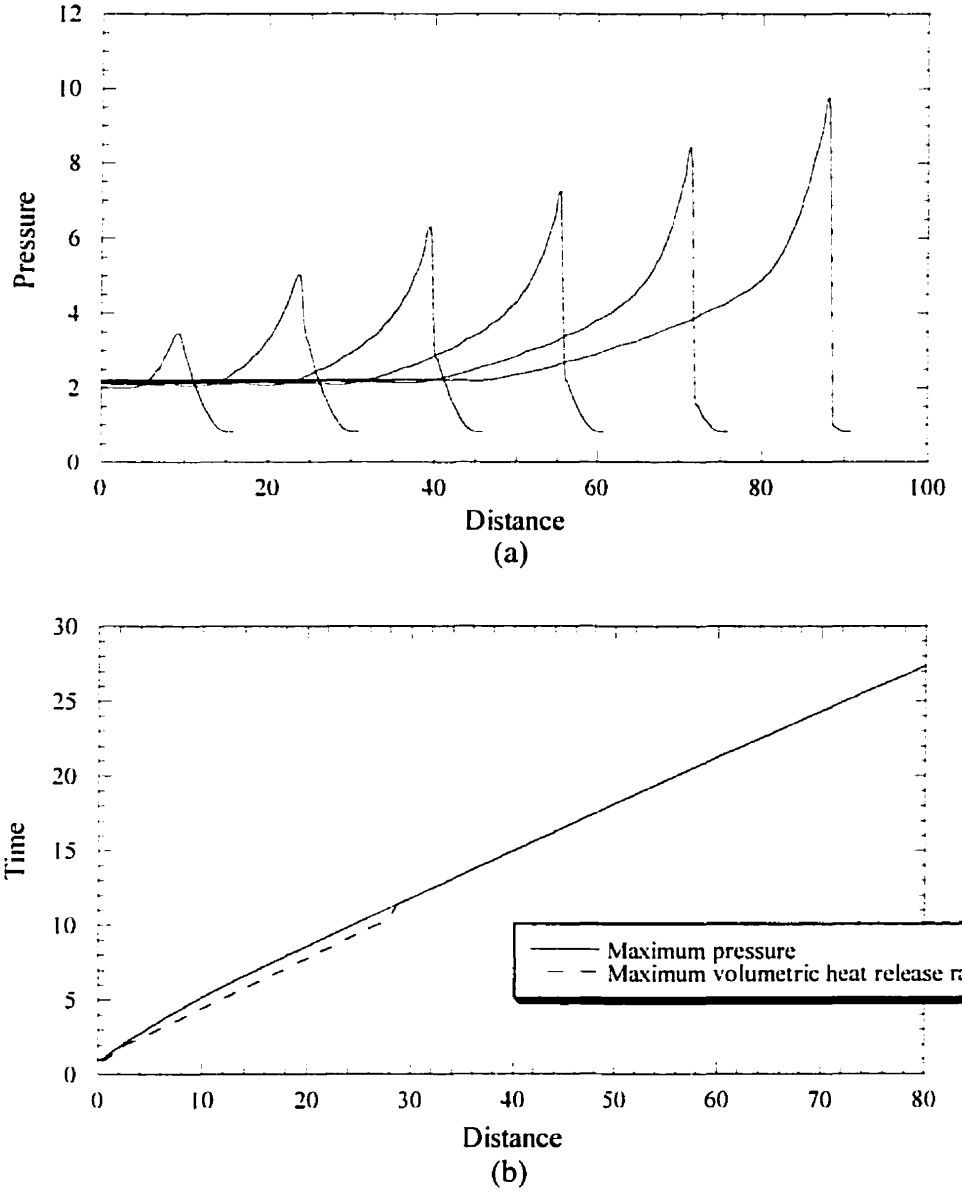

Figure 3.13: (a) Pressure profiles and (b) x-t diagram for $M_{source} = 3$.

On the other hand, pressure profiles (figure 3.13a) corresponded to the case of $M_{source} = 3$ clearly reveal a strong shock wave amplification. From figure

3.13b showing the trajectories of $(\rho\dot{q})_{max}$ and $(P)_{max}$, we can see more clearly the interaction between the pressure wave and the energy release. At $t \sim 10$, a shock wave is established and the shock raises the temperature, leading to a higher volumetric energy release rate. The reaction zone is then coupled with the pressure pulse, resulting in a strong shock wave amplification. Indeed, this energy source velocity corresponds closely to the C-J value of the mixture. Thereafter, the combustion front is always coupled with the compression wave.

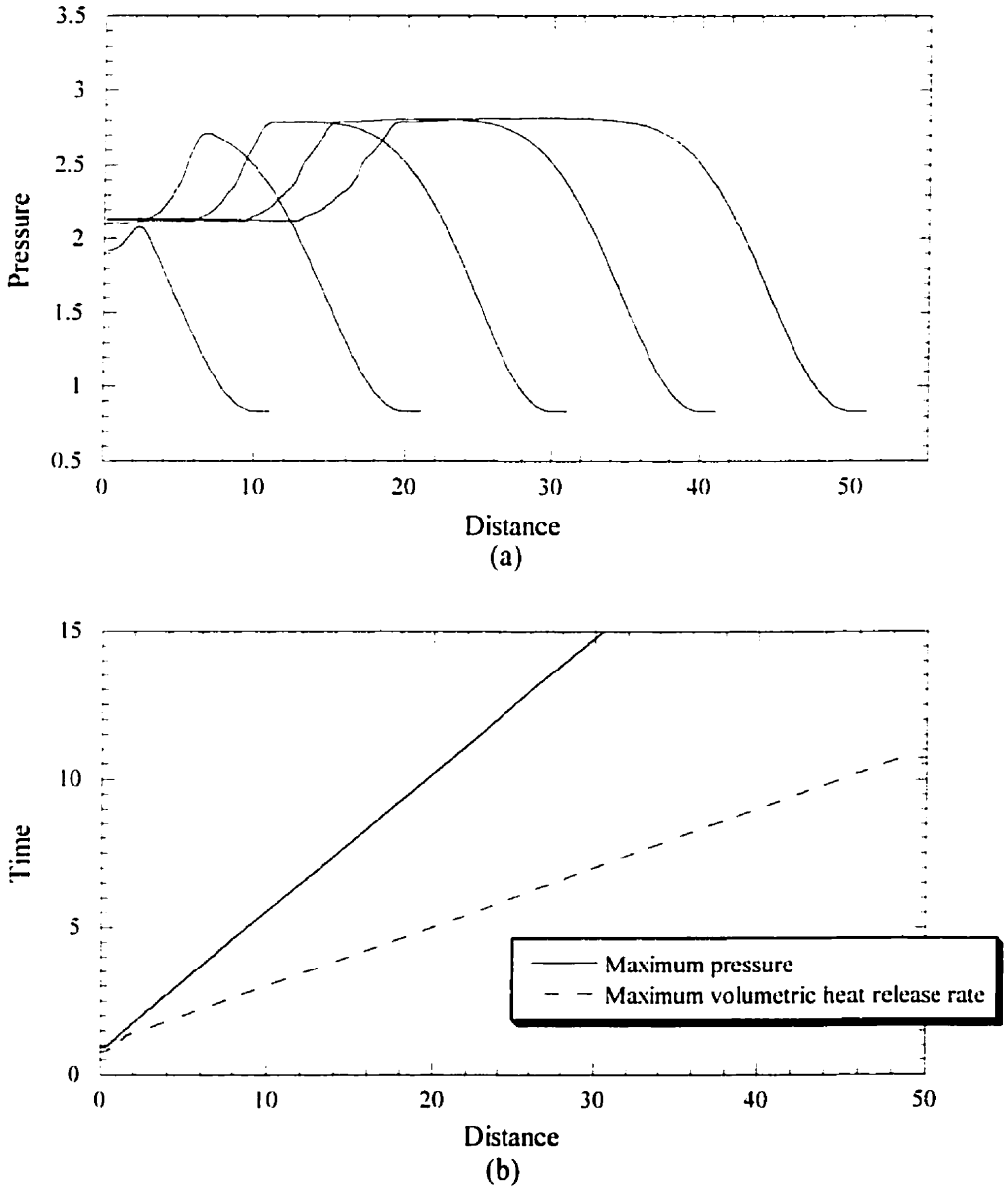

Figure 3.14: (a) Pressure profiles and (b) x-t diagram for $M_{source} = 5$.

If the source energy moves even faster, i.e., $M_{source} = 5$, it remains ahead of the compression wave as illustrated in the x-t diagram (figure 3.14b). As a result, no shock wave amplification can be seen in the pressure profiles as given in figure 3.14a. The compression wave broadens with time as the source travels into the undisturbed mixture. In the limit where M_{source} goes to infinite, it results in an uniform deposition of energy, which corresponds to a constant volume explosion.

The above example shows how a proper synchronization of the pressure pulse with the energy release can cause rapid amplification of the pressure pulse, resulting in the onset of a detonation. The time sequence of chemical energy release is such that it is coherent with the shock wave, thus adding strength to the shock wave as it propagates. When the pressure wave becomes strong enough to cause vigorous chemical reaction, the mixture will detonate. Therefore, effective shock wave amplification depends on whether or not a reacting flow-field maintains the SWACER mechanism for a sufficiently long duration. Various parameters, such as the induction time gradient, reactivity of gas mixture, or geometry of flow-field, should govern the SWACER mechanism.

3.4 The effect of instability on direct initiation

The initiation process for stable detonation was studied in the previous section. Similar calculations are presented here for unstable detonations. As mentioned in Chapter 2, if the induction length is increased relative to the recombination zone length, the detonation wave becomes unstable. We have introduced the ratio δ as the main parameter controlling the stability of one-dimensional pulsating detonations. An interesting question that arises is whether the instability of the detonation plays a role in the initiation processes.

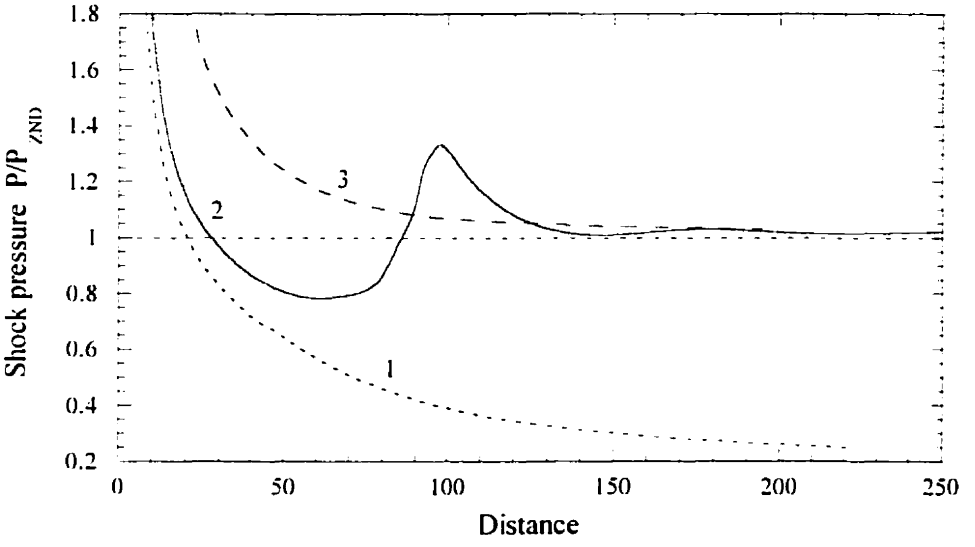

Figure 3.15: Shock pressure history for the direct initiation of a stable detonation with $\delta = 0.5652$ and different non-dimensional initiation energies: $E_{s1} = 342$, $E_{s2} = 370$ and $E_{s3} = 670$.

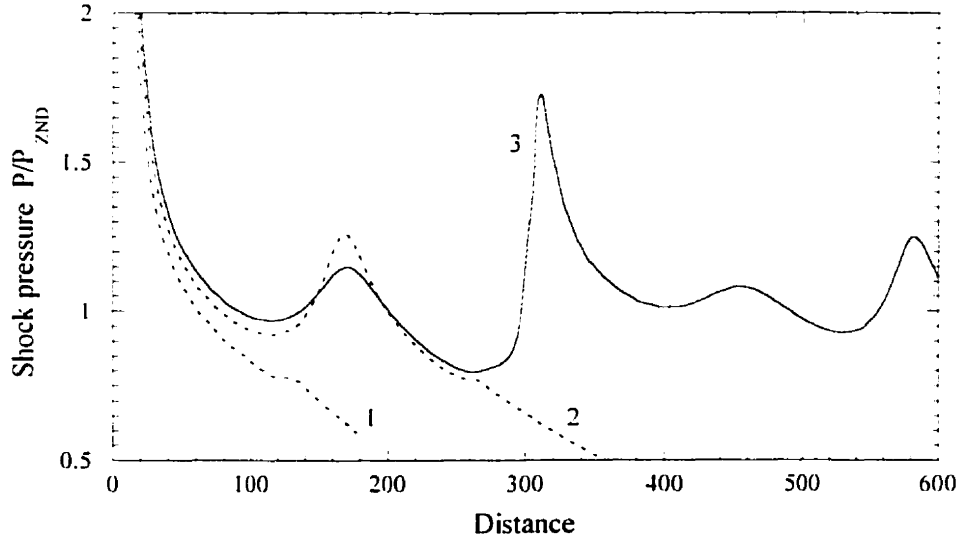

Figure 3.16: Shock pressure history for the direct initiation of a highly unstable detonation with $\delta = 1.1989$ and different non-dimensional initiation energies: $E_{s1} = 1370$, $E_{s2} = 1510$ and $E_{s3} = 1608$.

For comparison, figures 3.15 and 3.16 show the pressure history of the shock front for both stable and highly unstable detonation of planar geometry, respectively. For the stable case with $\delta = 0.5652$, the initiation process can be well described by the decay of the blast wave. The blast wave decays to a sub-CJ value and re-accelerates back to the C-J detonation after the quasi-steady period. Therefore, the critical initiation energy can be well approximated from the blast wave theory. The numerical result shows that some new phenomenon appears for highly unstable detonation ($\delta = 1.1989$), where the final self-sustained detonation propagates with a chaotic behavior. Instead the blast decaying continuously to the sub-CJ value, oscillation occurs during the initiation process. The detonation instability clearly influences the initiation process. For curve 1, the source energy is far from the critical value and the reaction front and shock front are decoupled throughout. The blast continues to decay to an acoustic wave. Curve 2 demonstrates how instability of the detonation front may induce some failure of the detonation. After the first oscillation of the shock pressure, it is possible that some unsteady event from the rear boundary of the reaction zone dominates the wave propagation and causes the quenching of the detonation wave. Therefore, a larger amount of initiation energy is expected to overcome all these instability effects of the detonation. The mechanism behind this initiation process for highly unstable detonation is beyond the scope of this work.

From these results we can see that the detonation instability is also important for the initiation process. So far, the instability effect has not been explicitly considered in any of the current initiation models. These models are mostly based on the blast wave theory and do not include a stability parameters in their formulations.

3.5 Other geometries

What we have considered so far is the initiation for planar detonations. For the planar case, the detonation wave is not subject to any curvature effect and only unsteadiness of the flow behind the shock causes the decay of the wave. For the cylindrical and spherical detonation, curvature will be a factor in addition to unsteadiness and we shall investigate these combined effects on the initiation process.

Curvature of a shock front induces an additional expansion of the gas behind it, and this additional expansion causes cooling and can lead to quenching of the reaction. When a fluid particle crosses a curved shock wave, it is first compressed by the shock and its temperature is increased. Subsequently, the compressed fluid particle expands volumetrically due to the radial, outward flow behind the shock and this expansion will result in a decrease in the temperature. This expansion can cause failure of the detonation if it is sufficiently rapid to quench the chemical reactions. To illustrate the curvature effect, consider the critical tube diameter phenomenon. When a detonation emerges abruptly from a confined tube into an open space, the planar detonation diffracts into a curved front. The wave fails if the curvature is excessive. Hence the tube diameter must be above some critical value so that the wave curvature does not lead to failure.

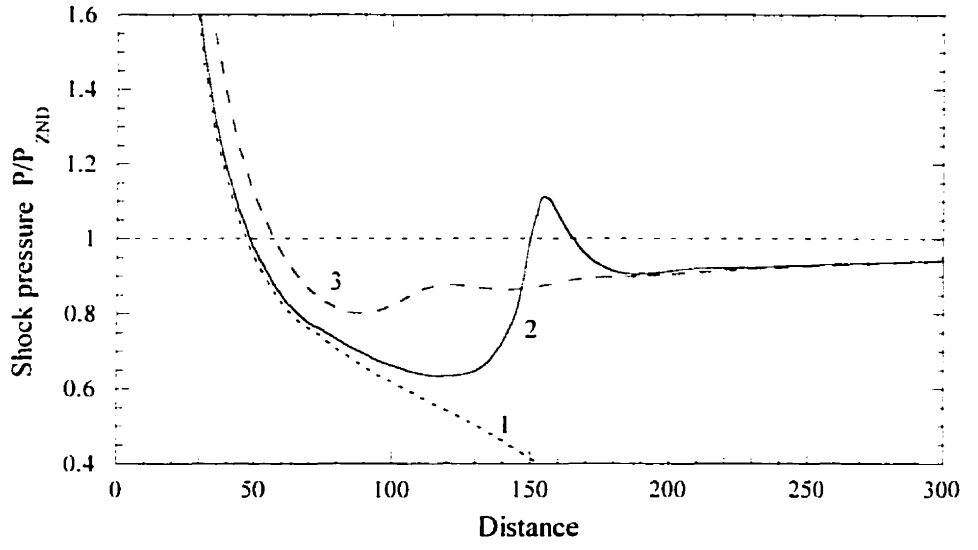

(a)

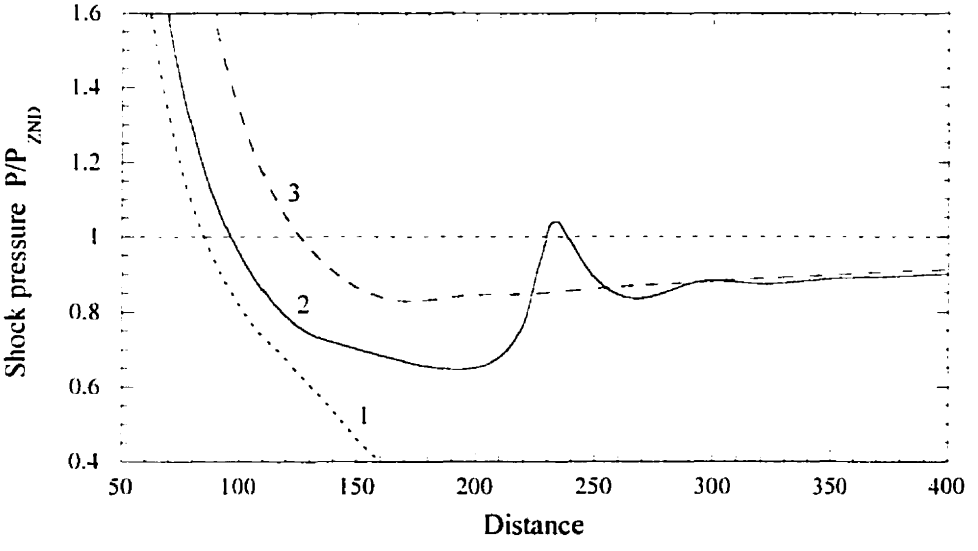

(b)

Figure 3.17: Three regimes of initiation for $Q = 10$, $\gamma = 1.2$ and $\delta = 0.5652$. (a) Cylindrical geometry with non-dimensional initiation energies: $E_{s1} = 8.96\text{x}10^4$, $E_{s2} = 9.34\text{x}10^4$ and $E_{s3} = 1.18\text{x}10^5$ (b) Spherical geometry with non-dimensional initiation energies: $E_{s1} = 3.30\text{x}10^7$, $E_{s2} = 4.74\text{x}10^7$ and $E_{s3} = 9.06\text{x}10^7$.

In the initiation of cylindrical and spherical detonation, the curvature decreases as the blast expands. However during the initiation process, both

curvature and unsteadiness effect can cause failure of the diverging wave. Figure 3.17 shows the shock pressure history for the three regimes of initiation for cylindrical and spherical geometries. Since curvature can cause additional quenching, initiation of cylindrical waves require that the same critical strength of blast to occur at a larger radius than the planar geometry. Similarly, spherical waves have even larger curvatures at the same radius. Hence, the same critical value of the strength of the blast must be maintained to even larger radius than the cylindrical geometry in order for successful initiation to be achieved.

The three regimes of initiation for stable detonation are qualitatively similar for all three geometries. The only difference is that for the planar geometry a self-sustained detonation is formed closer to the source. Another interesting result is that the detonation velocity is found to be slightly lower than the planar ZND solution. Since the curvature term goes like j/r in the conservation equations (j = 1, 2 for cylindrical and spherical geometries, respectively), then the velocity is always unsteady and only becomes CJ if the radius approach to infinity.

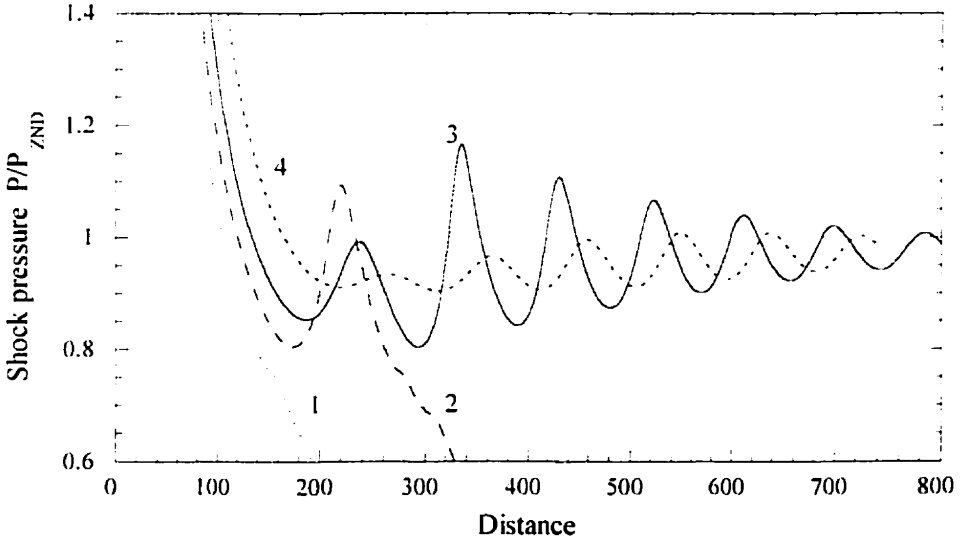

Figure 3.18: Direct initiation of unstable cylindrical detonation for Q = 10, γ = 1.2, δ = 0.8975 with non-dimensional initiation energies: $E_{s1} = 3.89\text{x}10^5$, $E_{s2} = 4.71\text{x}10^5$, $E_{s3} = 5.60\text{x}10^5$ and $E_{s4} = 7.63\text{x}10^5$.

Another interesting phenomenon for diverging wave is that curvature enhances instability of the detonation wave. Figure 3.18 shows the numerical results for a ratio $\delta = 0.8975$ for cylindrical geometry. Although this value of δ corresponds to a stable case for planar detonation (see Chapter 2), but in the case of cylindrical detonations, instability occurs when the radius of the front is small. For the curved detonation front, the particle undergoes an expansion behind the shock due to the curvature effect. This expansion due to curvature increases the induction time and hence enhances the instability of the detonation wave. This is even more significant for spherical detonation because of a higher curvature. The wave will become stable asymptotically when the radius approaches infinity.

3.6 The critical initiation energy

Previous numerical studies on direct initiation of detonation [30] based on a single-step Arrhenius rate law failed to yield a definitive value of the critical energy. This contradicts with experimental observation where a distinct value for the critical initiation energy is observed. To illustrate the problem of using a single rate law, the initiation processes for planar detonation for different initiation energies are plotted in figure 3.19. Note that if one waits long enough, then even curve "7" will eventually result in detonation initiation. Of course the time one has to wait increases exponentially, but no sharp cut off can be obtained with a single rate law to permit a unique value of the critical energy to be determined.

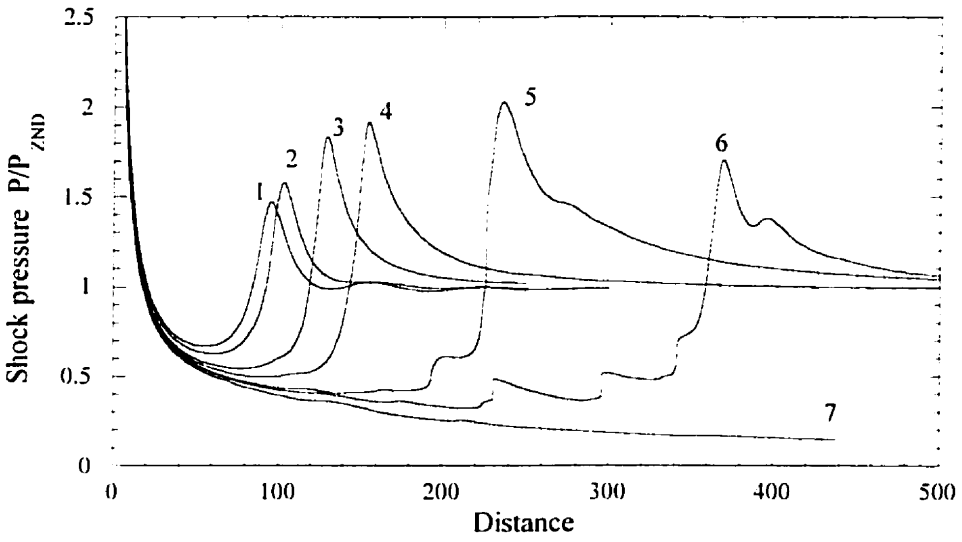

Figure 3.19: Shock pressure history for direct initiation using 1-step kinetic rate law for $Q = 50$, $\gamma = 1.2$ and $E_a = 24$ for different initiation energies: $E_{s1} = 3243$, $E_{s2} = 3285$, $E_{s3} = 3302$, $E_{s4} = 3361$, $E_{s5} = 3420$, $E_{s6} = 3601$ and $E_{s7} = 3724$.

However if a more realistic chemical kinetics model is used, the difficulty in identifying the critical energy can be eliminated. For instance, see figure 3.15. A single step rate model also does not provide a detonability limit. However using

a three-step reaction model. Short & Quirk [36] succeeded in obtaining a criterion for the detonability limit, i.e., onset of the detonability limit occurs when the shock temperature drops to the chain-branching cross-over temperature. For the direct initiation of detonation, a distinct value of the critical energy can be obtained if the blast generated by the source energy never drops below the chain-branching cross-over temperature T_B. If the energy is insufficient and the blast drops below the chain-branching cross-over temperature T_B, then the chain-branching reaction is effectively being switched off. Since the chain-branching induction length is now much longer than the recombination zone length, the rate of heat release is significantly reduced. In this case, the combustion front will no longer be able to couple with the leading shock and form a self-sustained detonation. Based on the chemical kinetics of the reactions, a criterion for defining the critical initiation energy can be obtained, i.e.,

> *"For successful initiation, the blast wave generated by the source must not drop below the chain-branching cross-over temperature before the onset of detonation occurs."*

Once it drops below this temperature limit, no initiation of detonation is possible. Thus, we see that the use of a three-step chain-branching reaction has a distinct advantage over the standard one-step Arrhenius model in that it can provide a "cut off" temperature and this leads to the possibility of obtaining a distinct value for the critical initiation energy.

Chapter 4

General Theories for Direct Initiation

4.1 Introduction

In the past two decades, several theories have been developed to estimate the critical initiation energy from a point source. Due to the non-uniqueness of the critical energy when a single-step Arrhenius rate law is used, these theories for direct initiation cannot be verified numerically from previous studies. Hence, it appears worthwhile to examine the validity of these theories from the results of present numerical simulations, where a more realistic chemical model is used.

4.2 Dependence of critical energy on induction length

A criterion for direct initiation was first proposed by Zel'dovich *et al.* [42]. For successful initiation, Zel'dovich stated that the blast radius should be on the order of the induction zone thickness by the time shock strength has decayed to the C-J value. From this argument, he demonstrated that the critical energy for direct initiation of spherical detonation must be proportional to the cube of the induction zone thickness, i.e., $E_s^* \sim \Delta^3$. Later, Lee [26] extended the Zel'dovich's initiation criterion to other geometries in the form of $E_s^* \sim \Delta^{j+1}$, where j = 0, 1, 2 for planar, cylindrical and spherical geometries, respectively. In the past forty years, most of the initiation models involve almost the same correlation between a characteristic chemical length and the critical initiation energy as described by Zel'dovich's model. Since Zel'dovich's criterion forms the base of many of these initiation models, thus it appears worthwhile to examine the validity of Zel'dovich's criterion for different geometries from the results of present numerical simulations using a more detailed chemical kinetics model, where a definitive value of the critical energy can be obtained.

The critical initiation energies for different geometries calculated by numerical simulations are plotted versus the induction zone length of the steady ZND detonation in figures 4.1. The corresponding induction zone length for detonability limit (above which no detonation can be formed) is also indicated in these figures. From these figures, it is shown that the critical initiation energy correlates well with the induction zone length as predicted by Zel'dovich's theory. The linear, quadratic and cubic correlation between the critical initiation energy and the ZND induction zone length for planar, cylindrical and spherical cases appear to be valid, especially for the case of short induction zone length, where the detonation is stable. For long induction zone length where the detonation is unstable, other effects such as curvature and non-steady expansion begin to influence the initiation process and the critical energy departs from the simple blast wave scaling law where Zel'dovich's theory is based. For all three geometries, it is observed that there is a small deviation from the Zel'dovich's criterion for long induction zone length. As mentioned previously, Zel'dovich's criterion simply relates the critical initiation energy with a chemical length scale, which does not include the effect of unsteadiness. Therefore, it is not appropriate to simply use the induction zone length for the very unsteady events in the initiation process. Furthermore, this deviation is more significant in cylindrical and spherical geometries because curvature appears to enhance the instability of the wave. Nevertheless, Zel'dovich's theory provides a mean to estimate the correct order of magnitude of the critical initiation energy.

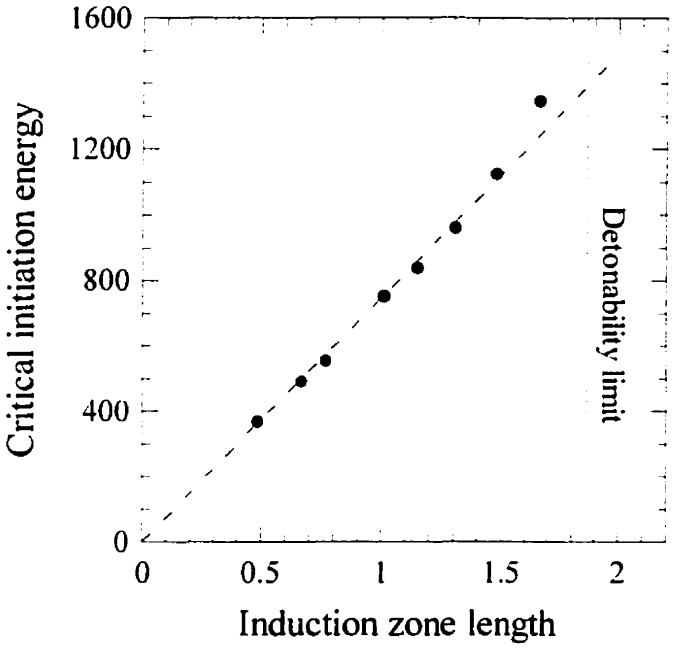
1600
1200
800
400
0
Critical initiation energy
0
0.5
1
1.5
2
Induction zone length
Detonability limit

(a)

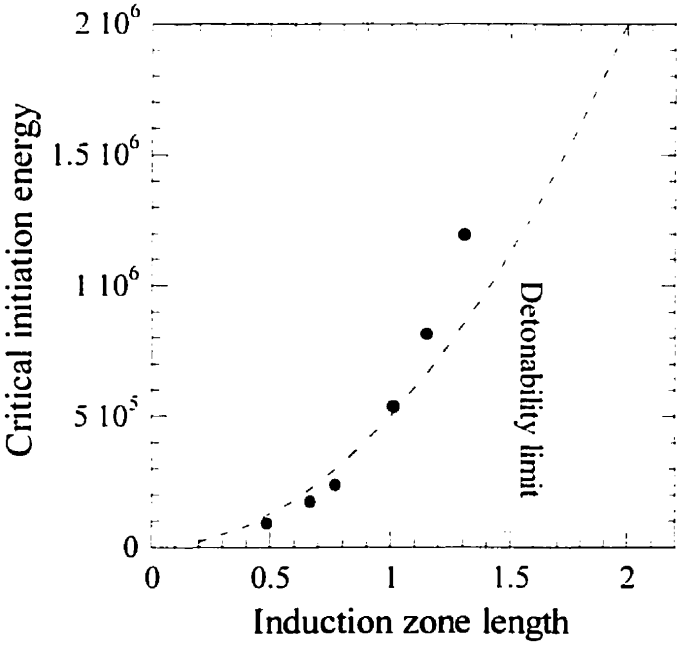
2 10^6
1.5 10^6
1 10^6
5 10^5
0
Critical initiation energy
0
0.5
1
1.5
2
Induction zone length
Detonability limit

(b)

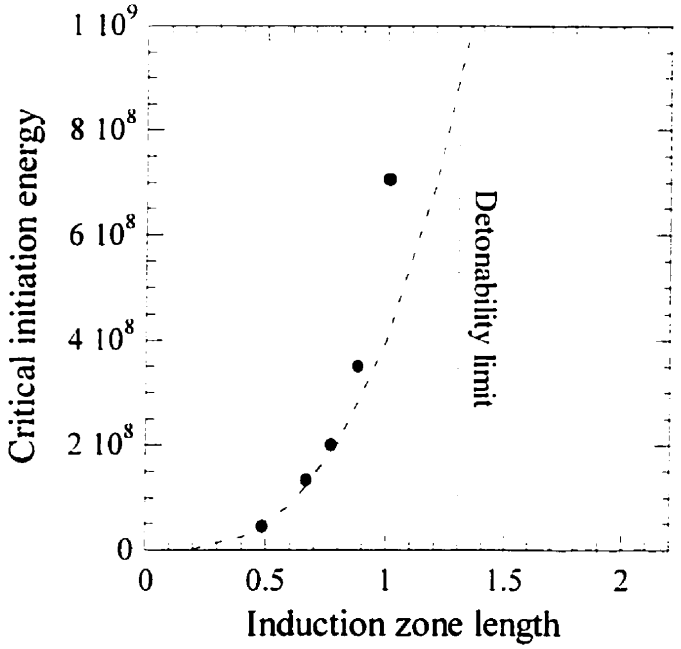

(c)

Figure 4.1: Variation of critical initiation energy with ZND induction zone length for (a) planar $j = 0$ (b) cylindrical $j = 1$ and (c) spherical $j = 2$ geometries. The dashed lines show the $E_s^* \sim \Delta^{j+1}$.

4.3 Invariance of the critical explosion length R_o

For direct initiation of detonation for different geometries, Lee [26] has suggested that the critical explosion length is independent of geometry.

$$R_o = \left(\frac{E_{\text{spherical}}}{P_o}\right)^{\frac{1}{3}} = \left(\frac{E_{\text{cylindrical}}}{P_o}\right)^{\frac{1}{2}} = \left(\frac{E_{\text{planar}}}{P_o}\right)^{1} \qquad (4.1)$$

The explosion length R_o represents a characteristic length of the source energy specific to the geometry and is the only length scale associated with strong blast decay. From the results of numerical simulations using the present 3-step chemical model for different geometries, it is also possible to verify the critical explosion length scaling law proposed by Lee. To do this, the critical explosion lengths for direct initiation in planar, cylindrical and spherical detonation are plotted in figure 4.2. From this figure, it is clear that the explosion length is

essentially invariant for all the three geometries for the same mixture parameters. Again, there is a small deviation for long induction zone length. As mentioned previously, this is due to the fact that the detonation becomes highly unstable for long induction zone length and the instability has a significant effect on the initiation process.

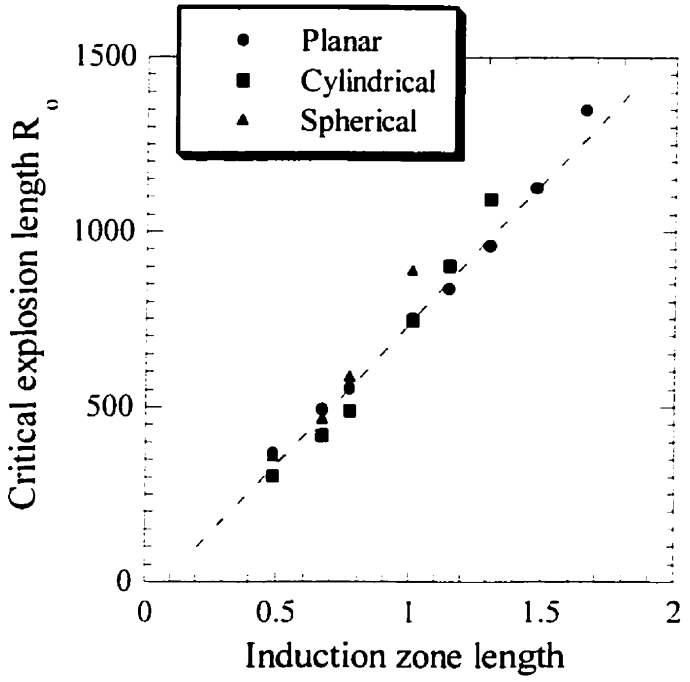

Figure 4.2: Invariance of explosion length for blast initiation for different geometries.

The invariance of the critical explosion length with geometry is quite useful in practice because we can predict the critical initiation energy for different geometries if it is known for one geometry. For example with the critical value of the explosion length known, then the critical initiation energy for different geometries could be determined, i.e.,

$$R_o = \frac{E_{\text{spherical}}}{E_{\text{cylindrical}}} = \frac{E_{\text{cylindrical}}}{E_{\text{planar}}} \tag{4.2}$$

Since the critical energy E_s^* is linked to the chemical length scale Δ of the detonation, i.e., $E_s^* \sim \Delta^{j+1}$, and from the explosion length invariance principle for different geometries, we could expect that the critical explosion length should also scale with the chemical length of the detonation, i.e., $R_o \sim \Delta$. In the present numerical study, the explosion length R_o under critical conditions is found to be in the order of $R_o \sim 810\Delta$.

Using the standard correlation between the cell size and induction length Δ of the form $\lambda \sim 30\Delta$ [39], the explosion length R_o under critical conditions can be roughly correlated with the cell size. In the present study, we obtain that R_o is in the order $R_o \sim 27\lambda$, which is close to some experimental results (i.e., R_o varies from $17 \sim 24\lambda$ for typical hydrocarbon-air -- Benedick *et al.* [5] and $R_o \sim 33\lambda$ in the recent study by Radulescu *et al.* [32])

4.4 Critical kernel radius R_s^* for direct initiation

The detonation kernel theory of Lee & Ramamurthi [29] states that there exists a critical size of detonation kernel for direct initiation. The size of the detonation kernel corresponds to the shock radius R_s* at which the shock wave has decayed to some critical Mach number M_s* before it re-accelerates back to a C-J detonation.

The appropriate choice of critical Mach number M_s* should reflect the critical shock strength below which any detonation would fail. The shock strength prior to the onset of detonation, during the so-called quasi-steady period, appears to be an appropriate value for the critical Mach number M_s*. Experimentally, the shock strength during the quasi-steady period is observed to be close to half the CJ detonation speed. The half-CJ value is generally accepted for the critical Mach number M_s* and is used in many initiation models [5]. However, this half-CJ value is only a general estimate from experimental observation and may disagree for different explosive mixtures. The present study suggests that the choice of critical Mach number should take into account the chemistry. In the previous

section, it is shown that if the blast wave generated by an initial point source drops below the chain-branching cross-over temperature T_B, initiation of detonation fails. Therefore, the shock temperature during the quasi-steady period should be close to this chain-branching cross-over temperature T_B. Hence, the shock strength to this temperature limit should be a more suitable choice of the critical Mach number M_s*, which corresponds to the shock strength very near the auto-ignition limit of a combustible mixture. Depending on the value of the chain-branching cross-over temperature T_B, the critical Mach number ranges from 0.5 ~ 0.9 M_{CJ}.

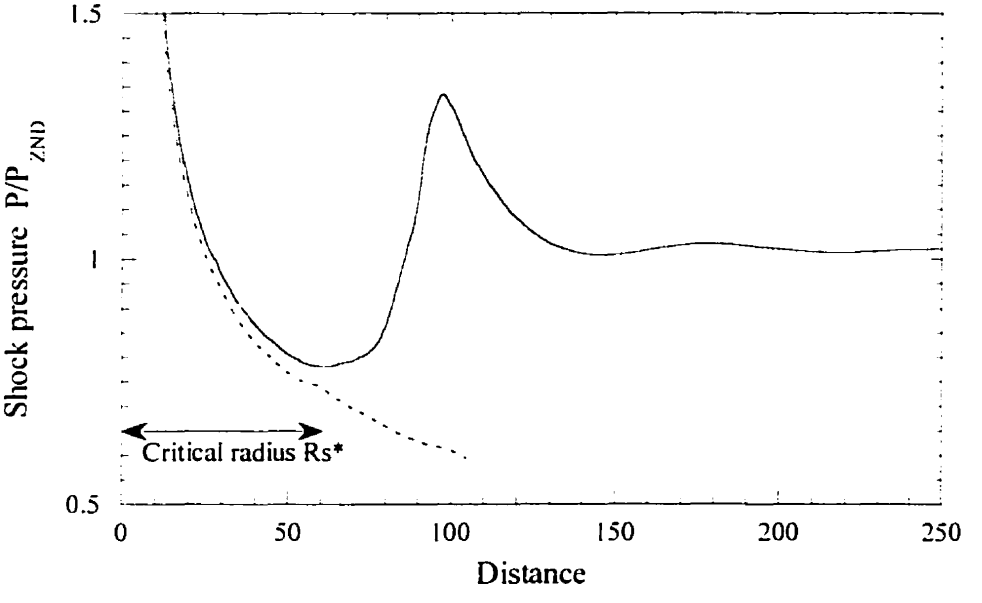

Figure 4.3: Definition of critical radius R_s^* from the numerical simulation of direct initiation.

In the present numerical results, the critical radius R_s^* is defined as the radius before the re-acceleration of the shock to detonation at the critical condition, as shown in figure 4.3. The value of critical radius R_s^* for different mixture from the present numerical simulations are given in Table 4.1.

Induction length Δ_1	R^*_{planar}/Δ_1	$R^*_{cylindrical}/\Delta_1$	$R^*_{spherical}/\Delta_1$
0.487	71.83	205.24	328.37
0.665	63.09	180.25	300.41
0.796	71.52	182.05	299.07
1.008	69.41	188.41	317.32
1.148	78.40	182.89	--
1.306	76.59	187.64	--
1.475	74.57	--	--
1.661	72.26	--	--

Table 4.1: Results of critical radius R_s^* for direct initiation from the present numerical simulations.

Conventionally, the critical kernel R_s^* at which the onset of detonation occurs is usually correlated to the cell size of the mixture, which is the most important dynamic parameter of gaseous detonation. Estimates of the critical radius for initiation vary widely in the literature. Table 4.2 shows some experimental results of critical radius for each geometry for typical hydrocarbon combustible mixture:

	R_s^*
Spherical	$\approx 10-13\ \lambda$ (Bull *et al.* [8])
Cylindrical	$\approx 4-8\ \lambda$ (Radulescu *et al.* [32])
Planar	less than $3\ \lambda$ (Benedick [4])

Table 4.2: Experimental results of critical kernel radius for different geometries.

For qualitative comparison between the results of the present numerical simulations, the standard correlation between the cell size and induction length Δ of the form $\lambda \sim 30\Delta$ is used once again. Using this correlation, we obtain the values of critical radius in term of cell size, i.e., $R_s^*_{planar} \sim 2.4\lambda$, $R_s^*_{cylindrical} \sim 6\lambda$ and $R_s^*_{spherical} \sim 10\lambda$. These results are in good agreement with the experimental results shown in Table 4.2.

Chapter 5
Conclusion

The problem of direct initiation using a more realistic multi-step chemical kinetics model has been investigated in the present thesis. A three-step chemical kinetics scheme used for this study represents the simplest realistic mechanism able to reproduce the essential dynamics of an actual chain-branching reaction. Due to the different mechanism of a chain-branching chemical reaction over a one-step global reaction, some differences between these two kinetics models are observed for the initiation and propagation of detonation.

This study demonstrates that using a more realistic chemical kinetics model could eliminate some of the difficulties in a single-step rate law and was able to more realistically reproduce the qualitative aspects of the direct initiation. Multi-step chemical kinetics model can provide a chemical switch-off mechanism that causes detonation failure to occur, which cannot be described by the one-step Arrhenius rate model. This permits a unique value for the critical initiation energy to be determined. A criterion for defining the critical initiation energy based on the chemical kinetics can also be obtained, due to the fact that the blast wave generated by the source must not decay below the chain-branching cross-over temperature before the onset of detonation occurs. Below this temperature limit, chain-branching reactions become ineffective, resulting in a sudden decrease in the global reaction rate and causing a quenching of energy release and a failure to initiate.

Due to the non-uniqueness of the critical energy when a single-step Arrhenius rate law is used, most of the existing theories on direct initiation cannot be verified numerically. In the present study where a more realistic chemical model is used and a clear cut-off value of critical energy can be obtained, these theories have been verified from the present numerical simulations. The

numerical results show that the detonation instability plays an important role in the initiation process. For a highly unstable mixture, results deviate from those obtained by prior theories for direct initiation. Since most of these existing initiation models are based on the blast wave theory, they do not include a parameter to model the detonation instability. This study suggests that the ratio δ between the induction and reaction zone length may be a good parameter to be include in the formulation of a theory for direct initiation to take into account for the effect of detonation instability. Regardless of the chemical reaction mechanism, this ratio δ is shown to control the detonation propagation. In addition, it is thought to govern the mechanism of the amplification process for initiation near the critical regime. A multi-step kinetics model is certainly required to investigate in more detail the effect of this ratio δ because it allows the independent variation of the induction and reaction length scales, which cannot be achieved by a single-step Arrhenius rate law. This permits us in future to perform a parametric study of these two length scales numerically and contribute in the development of a more vigorous theory for direct initiation.

In conclusion, this thesis justifies that the single-step rate law should be abandoned in favour of more detailed chemical kinetics model similar to the one employed in the present study for a more comprehensive study of the direct initiation of detonation.

References

1. Abouseif, G.E., and Toong, T.Y., Theory of unstable one-dimensional detonations, *Combust. Flame*, 45: 67-94, (1982)
2. Berger, M.J., and Colella, P., Local adaptive mesh refinement for shock hydrodynamics, *J. Comput. Phys.* 82: 64-84, (1989)
3. Bach, G.G., Knystautas, R., and Lee, J.H.S., Direct initiation of spherical detonations in gaseous explosives, *12th Symposium (Int.) on Combust.*, 21: 853-864, (1969)
4. Benedick, W.B., High-explosive initiation of methane-air detonations, *Combust. Flame*, 35: 87-91, (1979)
5. Benedick, W.B., Guirao, C., Knystautas, R., and Lee, J.H., Critical charge for the direct initiation of detonation in gaseous fuel-air mixtures, *Prog. Astro. Aero.*, 106: 181-202, (1985)
6. Borisov, A.A., Zamanskii, V.M., Lisyanskii, V.V., Heat evolution kinetics in high-temperature ignition of hydrocarbon/air or oxygen mixtures, *Prog. Astro. Aero.*, 114: 124-139, (1987)
7. Bourlioux, A., *Numerical Studies of Unstable Detonations*, PhD Thesis, Princeton University, (1991)
8. Bull, D.C., Elsworth, J.E., and Hooper, G., Initiation of spherical detonation in hydrocarbon/air mixtures, *Acta Astro.*, 5: 997-1008, (1978)
9. Chern, I.L., and Colella, P., A conservative front tracking method for hyperbolic conservation laws, *Lawrence Livermore National Laboratories Report No. UCRL-97200*, (1987)
10. Chue, R.S., *High Speed Deflagration and its Transition to Detonation*, PhD Thesis, McGill University, Montréal, Canada, (1993)
11. Colella, P., Glimm's method for gas dynamics, *SIAM J. Sci. Stat. Comput.*, 3: 76-109, (1982)
12. Colella, P., and Woodward, P.R., The piecewise parabolic method (PPM) for gas-dynamical simulations, *J. Comput. Phys.* 54: 174-201, (1984)

13. Dionne, J.-P., *Numerical Study of the Propagation of Non-ideal Detonations*, PhD Thesis, McGill University, Montréal, Canada, (2000)
14. Dionne, J.-P., Ng. H.D., Chue, R.S., and Lee, J.H.S., Numerical study of pathological detonations, *Proceedings of the 17th International Colloquium on the Dynamics of Explosions and Reactive Systems*, Universität Heidelberg, Germany, (1999)
15. Dold, J.W., and Kapila, A.K., Comparison between shock initiations of detonation using thermally-sensitive and chain-branching chemical models, *Combust. Flame*, 85: 185-194, (1991)
16. Eckett., C.A., Quirk, J.J., and Shepherd, J.E., An analytical model for direct initiation of gaseous detonations, *21st Symposium (Int.) on Shock Waves*, (1997)
17. Eckett., C.A., Quirk, J.J., and Shepherd, J.E., The role of unsteadiness in direct initiation of gaseous detonations, *J. Fluid Mech.*, 421: 147-183, (2000)
18. Erpenbeck, J.J., Stability of idealized one-reaction detonations, *Phys. Fluids*, 7: 684-696, (1964)
19. Fickett, W., Jacobson, J.D., and Schott, G.L., Calculated pulsating one-dimensional detonations with induction-zone kinetics, *AIAA J.*, 10: 514-516, (1972)
20. Fickett, W., and Wood, W.W., Flow calculation for pulsating one-dimensional detonations, *Phys. Fluids*, 9: 903-916, (1966)
21. He, L., Theoretical determination of the critical conditions for direct initiation of detonation in hydrogen-oxygen mixtures, *Combust. Flame*, 104: 401-418, (1996)
22. He, L., and Clavin, P., On the direct initiation of gaseous detonation by an energy source, *J. Fluid Mech.*, 277: 227-248, (1994)
23. He, L. and Lee, J.H., The dynamic limit of one-dimensional detonations, *Phys. Fluids*, 7: 1151-1158, (1995)
24. Lee, H.I., and Stewart, D.S., Calculation of linear detonation instability: One-dimensional instability of plane detonation, *J. Fluid Mech.*, 216: 103-132, (1990)
25. Lee, J.H.S., Dynamic parameters of gaseous detonations, *Ann. Rev. Fluid Mech.*, 16: 311-336, (1984)
26. Lee, J.H.S., Initiation of gaseous detonation, *Ann. Rev. Phys. Chem.*, 28: 75-104, (1977)

27. Lee, J.H.S., and Higgins, A.J., Comments on criteria for direct initiation of detonations, *Phil. Trans. R. Soc. Lond. A*, 357: 3503-3521, (1999)

28. Lee., J.H.S., and Moen, I.O., The mechanism of transition from deflagration to detonation in vapor cloud explosions, *Prog. Energy Combust. Sci.*, 6: 359-389, (1980)

29. Lee, J.H.S., and Ramamurthi, K., On the concept of the critical size of a detonatoin Kernel, *Combust. Flame*, 27: 331-440, (1976)

30. Mazaheri, B.K., *Mechanism of Onset of Detonation in Blast Initiation*, PhD Thesis, McGill University, Montréal, Canada, (1997)

31. Oran, E.S., and Boris, J.P., *Numerical Simulation of Reactive Flow*, Elsevier Science Publicating Co., Inc., (1987)

32. Radulescu, M.I., Higgins, A.J., and Lee, J.H.S., On the explosion length invariance in direct initiation of detonation, *28th Symposium (Int.) on Combust.*, University of Edinburgh, Scotland, (2000)

33. Sedov, L.I., *Similarity and Dimensional Methods in Mechanics*, 4th ed., Academic Press, New York, (1959)

34. Sharpe, G.J., Linear stability of idealized detonations, *Proc. R. Soc. Lond. A*, 453, 2603-2625, (1997)

35. Sharpe, G.J. and Falle, S.A.E.G., One-dimensional numerical simulations of idealized detonations, *Proc. R. Soc. Lond. A*, 455: 1203-1214, (1999)

36. Short, M., and Quirk, J.J., On the nonlinear stability and detonability limit of a detonation wave for a model three-step chain-branching reaction, *J. Fluid Mech.*, 339: 89-119, (1997)

37. Short, M., Kapila, A.K., and Quirk, J.J., The chemical-gas dynamic mechanisms of pulsating detonation wave instability, *Phil. Trans. R. Soc. Lond. A*, 357: 3621-3637, (1999)

38. Taylor, S.G., The formation of blast wave by a very intense explosion, I – Theoretical discussion, *Proc. Roy. Soc. A*, 201: 159-174, (1950)

39. Westbrook, C.K., and Urtiew, P.A., Chemical kinetic prediction of critical parameters in gaseous detonations, *19th Symposium (Int.) on Combust.*, 9: 615-623, (1982)

40. Westbrook, C.K., Chemical kinetics of hydrocarbon oxidation in gaseous detonations, *Combust. Flame*, 46: 191-210, (1982)

41. Yoshikawa, N., *Coherent Shock Wave Amplification in Photochemical Initiation of Gaseous Detonation*, PhD Thesis, McGill University, Montréal, Canada, (1980)

42. Zel'dovich, Ya. B., Kogarko, S.M., and Simonov, N.N., An experimental investigation of spherical detonation in gases, *Soviet Physics-Technical Physics*, 1: 1689-1713, (1957)

Appendix I: ZND Detonation Structure

The conservation equations

In a shock-fixed reference frame, the conservation equations (mass, momentum and energy) can be written as follows:

$$\frac{D}{v_o} = \frac{u}{v}$$

$$p_o + \frac{D^2}{v_o} = p + \frac{u^2}{v}$$

$$h_o + \frac{D^2}{2} = h + \frac{u^2}{2} - (Q - f \cdot Q - y \cdot Q)$$

We assume a polytropic equation of state, such that:

$$h = \frac{\gamma\ pv}{\gamma - 1}$$

and the equation for the conservation energy can be written as:

$$\frac{\gamma\ p_o v_o}{\gamma - 1} + \frac{D^2}{2} = \frac{\gamma\ pv}{\gamma - 1} + \frac{u^2}{2} - (Q - f \cdot Q - y \cdot Q)$$

The scales for density, pressure, temperature and velocity are the dimensional, initial pre-shock density, pressure, temperature and sound speed (with subscript o), respectively.

$$p' = \frac{p}{\gamma\ p_o} \quad v' = \frac{v}{v_o} \quad u' = \frac{u}{c_o} \quad M = \frac{D}{c_o} \quad \text{where } c_o^2 = \gamma\ p_o v_o$$

The scaled heat release quantity is defined as:

$$Q' = \frac{Q}{\gamma\ p_o v_o} = \frac{Q}{c_o^2}$$

Using the above non-dimensional variables, the conservation equations becomes:

Mass:

$$\frac{c_o}{v_o}\left(\frac{D}{c_o}\right) = \frac{c_o}{v_o}\left(\frac{v_o}{v}\right)\left(\frac{u}{c_o}\right) \rightarrow \left(\frac{D}{c_o}\right) = \left(\frac{v_o}{v}\right)\left(\frac{u}{c_o}\right) \rightarrow M = \frac{u'}{v'}$$

Momentum:

$$p_o + \frac{c_o^2}{v_o}\left(\frac{D}{c_o}\right)^2 = \gamma p_o\left(\frac{p}{\gamma p_o}\right) + \frac{c_o^2}{v_o}\left(\frac{u}{c_o}\right)^2\left(\frac{v_o}{v}\right)$$

$$\frac{1}{\gamma} + \frac{c_o^2}{\gamma\ p_o v_o}M^2 = p' + \frac{c_o^2}{\gamma\ p_o v_o}\frac{u'^2}{v'}$$

$$\frac{1}{\gamma} + \frac{\gamma\ p_o v_o}{\gamma\ p_o v_o}M^2 = p' + \frac{\gamma\ p_o v_o}{\gamma\ p_o v_o}\frac{u'^2}{v'} \quad \rightarrow \quad \frac{1}{\gamma} + M^2 = p' + \frac{u'^2}{v'}$$

Energy:

$$\frac{\gamma\ p_o v_o}{\gamma - 1} + \frac{c_o^2}{2}\left(\frac{D}{c_o}\right)^2 = \frac{\gamma^2\ p_o v_o}{\gamma - 1}\left(\frac{p}{\gamma p_o}\right)\left(\frac{v}{v_o}\right) + \frac{c_o^2}{2}\left(\frac{u}{c_o}\right)^2$$

$$-\gamma\ p_o v_o\left(\frac{Q}{\gamma\ p_o v_o} - f\cdot\frac{Q}{\gamma\ p_o v_o} - y\cdot\frac{Q}{\gamma\ p_o v_o}\right)$$

$$\frac{1}{\gamma - 1} + \frac{M^2}{2} = \frac{\gamma\ p'v'}{\gamma - 1} + \frac{u'^2}{2} - \left(Q' - f\cdot Q' - y\cdot Q'\right)$$

In summary, the conservation equations in non-dimensional form are:

$$M = \frac{u'}{v'}$$

$$\frac{1}{\gamma} + M^2 = p' + \frac{u'^2}{v'} = p' + Mu'$$

$$\frac{1}{\gamma - 1} + \frac{M^2}{2} = \frac{\gamma\ p'v'}{\gamma - 1} + \frac{u'^2}{2} - \left(Q' - f\cdot Q' - y\cdot Q'\right)$$

The Chapman-Jouguet state

At the C-J detonation state, the chemical energy is fully released and the products are in chemical equilibrium. Also, the flow velocity relative to the shock front is exactly sonic. This condition may be expressed as follows:

$$f = y = 0 \qquad u' = c' = \sqrt{\gamma\ p'v'}$$

Substituting these conditions into the conservation equations, we obtain:

$$M^2 = \frac{\gamma\ p'}{v'}$$

$$p' = \frac{1+\gamma\ M^2}{\gamma(\gamma+1)}$$

$$\frac{1}{\gamma-1} + \frac{M^2}{2} + Q' = \gamma\ p'v'\left(\frac{\gamma+1}{2(\gamma-1)}\right)$$

Substituting the momentum equation into the continuity equation, one can obtain:

$$v' = \frac{\gamma\ p'}{M^2} = \frac{1+\gamma\ M^2}{(\gamma+1)M^2}$$

Replacing the momentum and above equations into the energy equation gives:

$$\frac{1}{\gamma-1} + \frac{M^2}{2} + Q' = \left(\frac{1+\gamma\ M^2}{(\gamma+1)M}\right)^2\left(\frac{\gamma+1}{2(\gamma-1)}\right)\frac{1}{\gamma}\gamma$$

After some simplifications, one can obtain:

$$\boxed{\left(\frac{1}{2} - \frac{\gamma^{\,2}}{2(\gamma^{\,2}-1)}\right)X^2 + \left(\frac{1}{\gamma-1} + Q' - \frac{\gamma}{\gamma^{\,2}-1}\right)X - \left(\frac{1}{2(\gamma^{\,2}-1)}\right) = 0}$$

where $X = M^2$. The supersonic solution corresponds to the C-J detonation state. The subsonic solution corresponds to the C-J deflagration state. The other C-J state variables can be calculated using:

$$p' = \frac{1+\gamma\ M^2}{\gamma(\gamma+1)} \qquad v' = \frac{\gamma\ p'}{M^2} = \frac{1+\gamma\ M^2}{\gamma\ (\gamma+1)M^2}$$

The Von Neumann state

The state just behind the leading shock wave is called the Von Neumann state. It is used as the initial condition in the integration to find the flow properties in the reaction zone. Across the shock, no chemical reaction is occurred and thus:

$$f = 1 \quad \text{and} \quad y = 0$$

And the conservation equations becomes:

$$M = \frac{u'}{v'}$$

$$\frac{1}{\gamma} + M^2 = p' + \frac{u'^2}{v'} = p' + Mu'$$

$$\frac{1}{\gamma - 1} + \frac{M^2}{2} = \frac{\gamma\, p'v'}{\gamma - 1} + \frac{u'^2}{2}$$

Rearranging the mass and momentum equations, the followings can be obtained:

$$v' = \frac{u'}{M} \quad \text{and} \quad p' = \frac{1}{\gamma} + M^2 - Mu'$$

Putting these into the energy equation yields:

$$\frac{1}{\gamma - 1} + \frac{M^2}{2} = \frac{\gamma}{\gamma - 1}\left(\frac{1}{\gamma} + M^2 - Mu'\right)\frac{u'}{M} + \frac{u'^2}{2}$$

$$\frac{1}{\gamma - 1} + \frac{M^2}{2} = \frac{1}{\gamma - 1}\left(\frac{1 + \gamma\, M^2}{M}\right)u' - \left(\frac{\gamma}{\gamma - 1}\right)u'^2 + \frac{u'^2}{2}$$

$$\left(\frac{\gamma}{\gamma - 1} - \frac{1}{2}\right)u'^2 - \left(\frac{1 + \gamma\, M^2}{(\gamma - 1)M}\right)u' + \left(\frac{1}{\gamma - 1} + \frac{M^2}{2}\right) = 0$$

For a given Mach number, the above expression gives a quadratic equation with variable u':

$$\boxed{\left(\frac{\gamma + 1}{2(\gamma - 1)}\right)u'^2 - \left(\frac{1 + \gamma\, M^2}{(\gamma - 1)M}\right)u' + \left(\frac{1}{\gamma - 1} + \frac{M^2}{2}\right) = 0}$$

One solution is the trivial solution $u' = M$, the other corresponds to the Von Neumann particle velocity. Once the Von Neumann particle velocity is found, the other state variables can be calculated using:

$$v' = \frac{u'}{M} \qquad p' = \frac{1}{\gamma} + M^2 - Mu'$$

Reaction zone properties

To compute the reaction zone structure of the detonation, consider the two equations for the rate of consumption of fuel and radical:

$$\frac{df}{dt} = -w_I - w_B \quad , \quad \frac{dy}{dt} = w_I + w_B - w_c$$

These can be written as follows:

$$\frac{df}{dx}\frac{dx}{dt} = -w_I - w_B \quad \rightarrow \quad \frac{df}{dx} = \frac{-(w_I + w_B)}{u}$$

$$\frac{dy}{dx}\frac{dx}{dt} = w_I + w_B - w_C \quad \rightarrow \quad \frac{dy}{dx} = \frac{w_I + w_B - w_C}{u}$$

where:

$$w_I = f \exp\left(E_I\left(\frac{1}{T_I} - \frac{1}{T}\right)\right) \quad , \quad w_B = \rho\, f\, y \exp\left(E_B\left(\frac{1}{T_B} - \frac{1}{T}\right)\right) \quad , \quad w_C = y$$

and the variable x is the steady shock-attached distance coordinate system.

Given the initial condition which are the Von Neumann state, the above differential equations may be integrated away from the shock at $x = 0$ so as to determine the complete structure of the steady detonation wave for $x > 0$.

Numerical methods

The variation in the consumption progress variables is determined by 4th order Runge-Kutta method. The above differential equations have 2 dependent variable f and y:

$$\frac{df}{dx} = z(x, f, y)$$

$$\frac{dy}{dx} = g(x, f, y)$$

$$f(x_o) = f_o \quad , \quad y(x_o) = y_o$$

Here f_o and y_o are the initial conditions of the problem. Using a step size of h, the value of f and y can be found using:

$$f_1 = f_0 + \frac{1}{6}(k_1 + 2k_2 + 2k_3 + k_4) \quad ; \quad y_1 = y_0 + \frac{1}{6}(l_1 + 2l_2 + 2l_3 + l_4)$$

$$k_1 = h \cdot z(x_0, f_0, y_0) \quad ; \quad l_1 = h \cdot g(x_0, f_0, y_0)$$

$$k_2 = h \cdot z(x_0 + \frac{h}{2}, f_0 + \frac{k_1}{2}, y_0 + \frac{l_1}{2}) \quad ; \quad l_2 = h \cdot g(x_0 + \frac{h}{2}, f_0 + \frac{k_1}{2}, y_0 + \frac{l_1}{2})$$

$$k_3 = h \cdot z(x_0 + \frac{h}{2}, f_0 + \frac{k_2}{2}, y_0 + \frac{l_2}{2}) \quad ; \quad l_3 = h \cdot g(x_0 + \frac{h}{2}, f_0 + \frac{k_2}{2}, y_0 + \frac{l_2}{2})$$

$$k_4 = h \cdot z(x_0 + h, f_0 + k_3, y_0 + l_3) \quad ; \quad l_4 = h \cdot g(x_0 + h, f_0 + k_3, y_0 + l_3)$$

The mass fraction f and y are evaluated numerically using Runge-Kutta method and the other state variables are evaluated directly from the 3 conservation equations for each step size h.

Consider again the 3 conservation equations:

$$M = \frac{u'}{v'}$$

$$\frac{1}{\gamma} + M^2 = p' + \frac{u'^2}{v'} = p' + Mu'$$

$$\frac{1}{\gamma - 1} + \frac{M^2}{2} = \frac{\gamma\, p'v'}{\gamma - 1} + \frac{u'^2}{2} - (Q' - f \cdot Q' - y \cdot Q')$$

From the continuity and momentum equation:

$$u' = Mv'$$

$$p' = \frac{1}{\gamma} + M^2 - Mu'$$

Substitute these relations into the energy equation, one can obtain:

$$\frac{1}{\gamma - 1} + \frac{M^2}{2} = \frac{(1 + \gamma M^2 - \gamma M^2 v')v'}{\gamma - 1} + \frac{M^2 v^2}{2} - (Q' - f \cdot Q' - y \cdot Q')$$

$$\frac{1}{\gamma - 1} + \frac{M^2}{2} = \frac{v' + \gamma M^2 v' - \gamma M^2 v'^2}{\gamma - 1} + \frac{M^2 v^2}{2} - (Q' - f \cdot Q' - y \cdot Q')$$

$$\frac{1}{\gamma - 1} + \frac{M^2}{2} = \frac{v'}{\gamma - 1} + \frac{\gamma M^2 v'}{\gamma - 1} - \frac{\gamma M^2 v'^2}{\gamma - 1} + \frac{M^2 v^2}{2} - (Q' - f \cdot Q' - y \cdot Q')$$

Given the Mach number of the detonation wave, the above equation is a quadratic equation in v':

$$v'^2\left(\frac{M^2}{2}-\frac{\gamma M^2}{\gamma-1}\right)+v\left(\frac{1}{\gamma-1}+\frac{\gamma M^2}{\gamma-1}\right)-\left((Q'-f\cdot Q'-y\cdot Q')+\frac{1}{\gamma-1}+\frac{M^2}{2}\right)=0$$

The other state variables can be computed using:

$$p'=\frac{1}{\gamma}+M^2-M^2v \qquad u'=Mv'$$

These equations are used to update the state variables inside the reaction zone for each step size h. These values will be used for the next integration step of the rate equations.

Appendix II: Numerical Methods

Fractional steps method

We are solving the reactive Euler equation in conservation form:

$$U_t + F(U)_x = S - JG \tag{A1}$$

where U, $F(U)$, S, G denote the flow vector, the flux, the source term due to combustion and geometry, respectively. J is the geometric index (J = 0, 1, 2 for planar, cylindrical and spherical geometries, respectively)

The system is solved by the use of a splitting scheme where the hydrodynamics transport and the chemical effects are taken into account separately in successive fractional steps. Basically, we divide the problem into several sub-problems. The fractional step technique proceeds as follows. In the first step, we solve the non-reactive version of equation A1 by setting all the source terms to zero:

$$U_t + F(U)_x = 0 \tag{A2}$$

The solution of equation A2 serves as the initial condition for the system of ordinary differential equations for the geometrical source terms:

$$U_t = -JG \tag{A3}$$

Finally, we use the solution of equation A3 as the initial condition to solve the equation for the source term due to chemical reaction.

$$U_t = S \tag{A4}$$

The solution to equation A4 completes the solution at the new time level. A complete second order accurate splitting scheme (Strang's splitting method) to integrate from t^n to t^{n+1} is of the form:

$$U^{n+1} = L_H^{(\frac{1}{2}\Delta t)} L_G^{(\frac{1}{2}\Delta t)} L_C^{\Delta t} L_G^{(\frac{1}{2}\Delta t)} L_H^{(\frac{1}{2}\Delta t)} U^n$$

where $L_H^{\Delta t}$ denotes the finite difference approximation operator for the hyperbolic equation A2. $L_G^{\Delta t}$ and $L_C^{\Delta t}$ are discrete operators for the ordinary equations A3 and A4 for the geometric and chemical source term, respectively.

Hydrodynamic solver: PPM method

In the above numerical scheme, the hydrodynamic equation (equation. A2) is solved using the piecewise parabolic method of Colella & Woodward [12], which is a higher-order extension of Godunov's method. The flow variables U are updated using the following discrete conservative form:

$$U_i^{n+1} = U_i^n - \frac{\Delta t}{\Delta x}(F_{i+1/2} - F_{i-1/2})$$

where $\Delta x = x_{i+1/2} - x_{i-1/2}$ and $\Delta t = t^{n+1} - t^n$. F is the flux at the interfaces between two cells. To find the solution U at a new time level t^{n+1}, the interface fluxes $F_{i+1/2}$ and $F_{i-1/2}$ must be properly determined. The difference between different numerical schemes is to how to obtain these fluxes. The above update formula is conservative no matter how we define our numerical flux F. It is therefore possible to create a multitude of conservation methods simply by defining the inter-cell fluxes differently and using the above update formula. For Godunov method, instead of using some averaging between cells values, the fluxes are computed from an exact solution of Riemann problem at the interface between two adjacent cells. For PPM method, instead of using a constant value for the dependent variable at each cell as in the Godunov method, uses a parabolic interpolation in each cell of the form:

$$U(x) = U_{i-1/2} + \xi[\Delta U_i + U_{6,i}(1-\xi)]$$

where,

$$\xi = \frac{(x - x_i)}{\Delta x} \qquad x_{i-1/2} \le x \le x_{i+1/2}$$

$$\Delta U_i = U_{i+1/2,L} - U_{i-1/2,R} \quad \text{and} \quad U_{6,i} = 6[U_i - \frac{1}{2}(U_{i+1/2,L} + U_{i-1/2,R})]$$

We obtain $U_{i+1/2,L}$ and $U_{i+1/2,R}$ by first using an interpolation scheme to calculate $U(x)$ and an approximation to the value of U at $x_{i+1/2}$, subject to the constraint that $U_{i+1/2}$ does not fall out of the range of values given by U_i and $U_{i+1/2}$. The interface value is calculated as:

$$U_{i+1/2} = \frac{1}{2}(U_{i+1} + U_i) + \frac{1}{6}(\delta_i U_i - \delta_i U_{i+1})$$

where

$$\delta_i U_i = \min(|\delta U_i|, 2|\Delta_{i+1/2}|, 2|\Delta_{i-1/2}|)\,sign(\delta U_i), \quad \text{if} \quad \Delta_{i+1/2} \cdot \Delta_{i-1/2} > 0$$

$\delta_l U_i = 0$ otherwise.

with $\delta U_i = \frac{1}{2}(U_{i+1} - U_{i-1})$ $\Delta_{i+1/2} = U''_{i+1} - U''_i$ $\Delta_{i-1/2} = U''_i - U''_{i-1}$

In smooth parts of the solution, away from extrema, the left and right states can be obtained as:

$$U_{i+1/2,L} = U_{i+1/2,R} = U_{i+1/2}$$

so that the interpolation function $U(x)$ is continuous at the interface. In some cases, the interpolation function $U(x)$ takes on values which are not between $U_{i+1/2,L}$ and $U_{i+1/2,R}$. Therefore, the value $U_{i+1/2,L}$ and $U_{i+1/2,R}$ are further modified such that $U(x)$ is monotone function on each cell $(x_{j-1/2}, x_{j+1/2})$. The new expressions for $U_{i+1/2,L}$ and $U_{i+1/2,R}$ are thus written as:

$U_{i,L} = U_{i,R} = U''_i$ if $(U_{i,R} - U''_i)(U''_i - U_{i,L}) \le 0$

$U_{i,L} = 3U''_i - 2U_{i,R}$ if $(U_{i,R} - U_{i,L})[U''_i - \frac{1}{2}(U_{i,R} + U_{i,L})] > \frac{(U_{i,R} - U_{i,L})^2}{6}$

$U_{i,R} = 3U''_i - 2U_{i,L}$ if $-\frac{(U_{i,R} - U_{i,L})^2}{6} > (U_{i,R} - U_{i,L})[U''_i - \frac{1}{2}(U_{i,R} + U_{i,L})]$

Once we have these values $U_{i,L}$ and $U_{i,R}$, the cell interface fluxes can be obtained by:

$$F_{i+1/2,L}(y) = U_{i,R} - \frac{x}{2}[\Delta U_i - (1 - \frac{2}{3}x)U_{6,i}] \qquad x = \frac{y}{\Delta\xi_i}$$

$$F_{i+1/2,R}(y) = U_{i+1,L} - \frac{x}{2}[\Delta U_{i+1} + (1 - \frac{2}{3}x)U_{6,i+1}] \qquad x = \frac{y}{\Delta\xi_{i+1}}$$

Once the left and right states at interface are known, the next step is to solve the Riemann problem to obtain the value of flow variables at interface. Details of the PPM method are given in the papers by Collela & Woodward [12] and Mazaheri [30].

Shock front tracking

For the simulation of unstable detonations, the leading shock front must be computed very accurately. Thus, a tracking procedure is implemented in the present algorithm. The present numerical scheme used a simplest conservative front tracking by Chern & Colella [9]. The details of this method to track a shock wave moving to the right into an uniform flow U_0 is described next and illustrated in figure A.1.

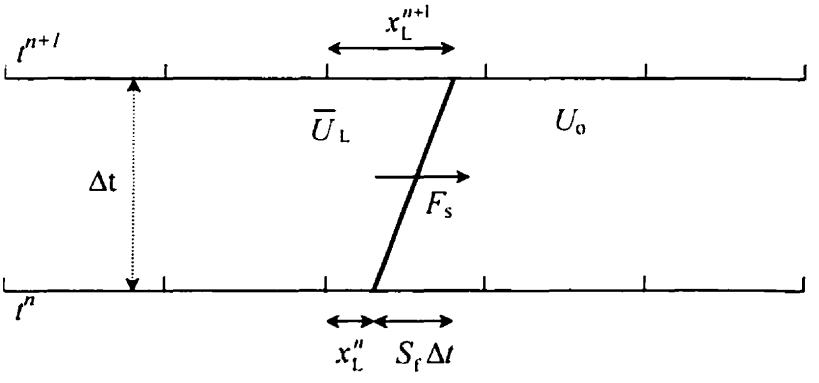

Figure A.1: Update of the shock location.

At time t^n, the solution U_i^n at all cells is known. In addition, the position of the tracked front X_{Sh}^n is known as well, which is located in cell i_{sh}. The shock front divides this cell i_{sh} into two subintervals. The average of U is also known on those two subintervals. The pre-shock values U_R^n and U_i^n for those cells ahead of the shock are equal to the constant state U_0 and do not need to be updated. The average value of the conservative variable U at the left subinterval $\overline{U}_L$ is computed by:

$$\overline{U}_L = U_L^n \frac{x_L^n}{\Delta x} + U_{i_{sh}-1}^n (1 - \frac{x_L^n}{\Delta x})$$

where x_L is the length of left subinterval of the cell i_{sh} which contains the shock. The front speed S_f is calculated using the Rankine-Hugoniot relationship for a normal shock separating left and right states:

$$S_f = [\frac{\gamma P_R}{\rho_R}(1 + \frac{\gamma+1}{2\gamma}(\frac{\overline{P}_L - P_R}{P_R}))]^{\frac{1}{2}} + U_R$$

and the shock position is updated by:

$$x_{Sh}^{n+1} = x_{Sh}^{n} + S_f \Delta t$$

The flux across the front is also computed by:

$$F_s = F(U_o) - S_f U_o$$

The flow behind the shock is updated. The PPM algorithm is applied in all cells for $i<i_{Sh}$. However a special treatment is needed for the cell containing the shock front. There are two possible cases and the conservative variable for this cell containing the shock can be updated as follows.

Case 1) $i_{Sh}^{n+1} = i_{Sh}^{n}$

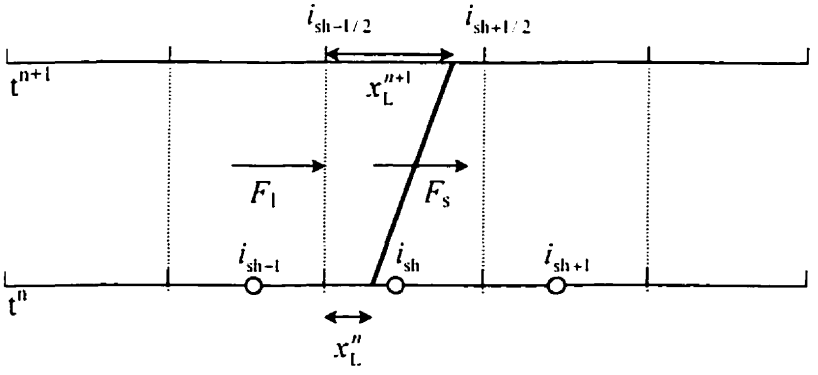

Figure A.2: Shock front tracking for $i_{Sh}^{n+1} = i_{Sh}^{n}$.

The conservative update of U for the left subinterval between t^n and t^{n+1} may be written in this form:

$$x_L^{n+1} U_L^{n+1} = x_L^n U_L^n + \Delta t(F_l - F_s)$$

This is not a stable way to updating U_L because if x_L^{n+1} is very small, the CFL condition will be violated [7]. This is the major difficulty with front tracking procedures. To resolve this problem, Chern & Colella's method (flux redistribution near the front) suggested the following procedure:

$$x_L^{n+1} U_L^{n+1} = x_L^n U_L^n + \Delta t(F_l - F_s) + x_L^{n+1} U_L^n - x_L^{n+1} U_L^n$$

$$x_L^{n+1} U_L^{n+1} = x_L^{n+1} U_L^n + \Delta t(F_l - F_s) + (x_L^n - x_L^{n+1}) U_L^n$$

Denote:

$$\delta M_L = (x_L^n - x_L^{n+1})U_L^n + \Delta t(F_1 - F_s)$$

therefore,

$$x_L^{n+1}U_L^{n+1} = x_L^{n+1}U_L^n + \delta M_L \tag{A5}$$

To avoid the violation of CFL stability condition, δM_L is divided into two parts:

$$\delta M_L = \frac{x_L^{n+1}}{\Delta x}\delta M_L + (1 - \frac{x_L^{n+1}}{\Delta x})\delta M_L = \delta M_{L1} + \delta M_{L2}$$

Substituting it in equation A5, we obtained:

$$U_L^{n+1} = U_L^n + \frac{\delta M_L}{\Delta x}$$

To maintain strict conservation, the remaining flux δM_{L2} is re-distributed between left subinterval of i_{Sh} and its left cell i_{Sh-1}. The general procedure redistributes it among the cells based on the flux decomposition in terms of eigenvectors, so that its various components are distributed to where they are being propagated in the sense of characteristics. In the present case of a shock wave moving into an uniform flow, the redistribution formulas are very simple:

$$U_L^{n+1} = U_L^{n+1} + \frac{1}{\Delta x + x_L^{n+1}}\delta M_{L2}$$

$$U_{i_{Sh}-1}^{n+1} = U_{i_{Sh}-1}^{n+1} + \frac{1}{\Delta x + x_L^{n+1}}\delta M_{L2}$$

Case 2) $i_{Sh}^{n+1} = i_{Sh}^n + 1$

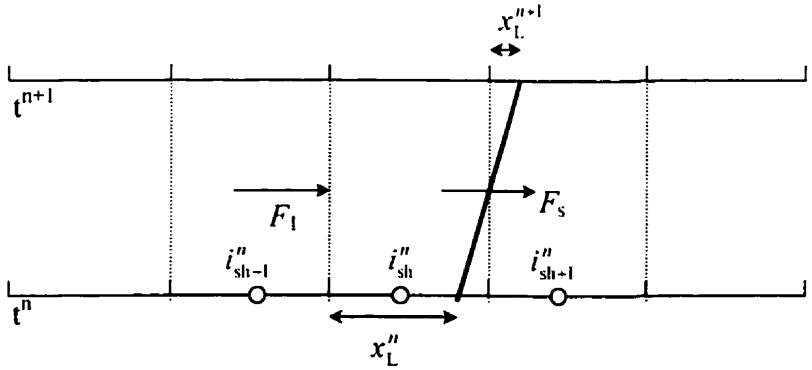

Figure A.3: Shock front tracking for $i_{Sh}^{n+1} = i_{Sh}^n + 1$.

This situation is slightly more complicated than case 1. First of all, the fraction of Δt which is elapsed in the new cell containing the shock, called it τ, is introduced as:

$$\tau = \frac{x_L^{n+1}}{S_f}$$

Then, the conservation equations will be applied in two steps in the shocked cell. Once between t^n and $t^n+(\Delta t-\tau)$, and then between $t^n+(\Delta t-\tau)$ and t^{n+1}. The conservation law is applied for both cells i_{Sh}^n and i_{Sh}^{n+1}.

$$\Delta x U_{i_{Sh}^n}^{n+1} = x_L^n U_L^n + \Delta t F_1 - \tau \overline{F} - (\Delta t - \tau) F_s$$

$$x_L^{n+1} U_L^{n+1} = \tau(\overline{F} - F_s)$$

where, $\overline{F} = F(\overline{U}_L)$. Similar to case 1, we derive the following expressions:

$$x_L^{n+1} U_L^{n+1} = x_L^{n+1} \overline{U}_L - x_L^{n+1} \overline{U}_L + \tau(\overline{F} - F_s)$$

and denote δM_L as:

$$\delta M_L \frac{x_L^{n+1}}{\Delta x} \delta M_L + (1 - \frac{x_L^{n+1}}{\Delta x}) \delta M_L = \delta M_{L1} + \delta M_{L2}$$

then,

$$U_L^{n+1} = \overline{U}_L + \frac{\delta M_L}{\Delta x}$$

and finally the same method of redistribution of δM_{L2} as in case 1:

$$U_L^{n+1} = U_L^{n+1} + \frac{1}{\Delta x + x_L^{n+1}} \delta M_{L2}$$

$$U_{i_{Sh}^n}^{n+1} = U_{i_{Sh}^n}^{n+1} + \frac{1}{\Delta x + x_L^{n+1}} \delta M_{L2}$$

Adaptive mesh refinement

In the present numerical scheme, the adaptive mesh refinement technique of Berger & Collela [2] is used to resolve effectively the region near the shock front. Two uniform grids are used to cover the computational domain. The entire domain is covered by a basic coarse grid and a fine mesh is superimposed on the coarse grid in the vicinity of the leading front. Find grid boundaries always coincide with coarse grid cell boundaries.

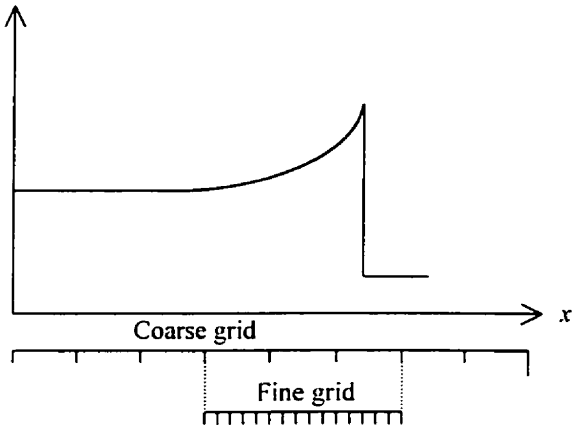

Figure A.4: Adaptive mesh refinement.

Given the solution on both grids at time t^n, the complete solution at next time level $t^{n+1}=t^n+\Delta t$ is obtained via the following procedures:

1. The flow variables in the coarse grids are first updated with time step Δt^C.
2. Next, the solution in the fine grids is updated. Denote N_R to be the refinement ratio between the coarse and fine grid mesh sizes, then N_R successive integrations are required on the fine grids with time step $\Delta t^f = \Delta t^C/N_R$.
3. Information from the fine grids needs to be fed back into the coarse grids. Therefore, those coarse grids superimposed by fine meshes are updated again. Finally, the values of the flow variables are replaced by the conservative average of the corresponding values of the fine grid points within them.

4. The location of the shock front on the coarse grid is also replaced by its value on the fine grid.
5. To preserve strict conservation, the solution at the left boundary of the fine grid is corrected by the following formula:

$$\Delta x U_{i_L-1}^{c,n+1} = \Delta x U_{i_L-1}^{c,n+1} + \Delta t F_L^c - \sum_{N_R} \frac{\Delta t}{N_R} F_L^f$$

where F_L^c is the flux at the interface between the coarse and fine grids determined previously in step 1, F_L^f is the flux at the same place calculated in step 2, and $U_{i_L-1}^{c,n+1}$ is the conservative variable on the first coarse cell at the left of the interface between coarse and fine meshes [7, 30].

6. The position of the fine grid with respect to the coarse grid is finally updated to account for the motion of the tracked shock. The fine grid is located such that the tracked leading shock is always covered by the fine grid.